Pore formation at the lytic synapse triggers the canonical pyroptotic cell death pathway

Authors: Brienne McKenzie[1*], Marie-Pierre Puissegur[1], Lucie Demeersseman[1], Frecia Rodriguez[1], Emma Cini[1], Sabina Müller[1], Salvatore Valitutti[1,2*]

Affiliations:

[1]Institut National de la Santé et de la Recherche Médicale (INSERM) UMR1037, Centre de Recherche en Cancérologie de Toulouse (CRCT), Toulouse, France.
Centre National de la Recherche Scientifique (CNRS) UMR5071, Toulouse, France
Université de Toulouse III-Paul Sabatier, 31037 Toulouse, France

[2] Department of Pathology, Institut Universitaire du Cancer-Oncopole de Toulouse (IUCT), Toulouse, France

Keywords: cyotoxic T lymphocytes, pyroptosis, programmed cell death, caspase-1, gasdermin D, perforin

***Corresponding authors:** brienne.mckenzie@inserm.fr

SUMMARY

Antigen-specific cytotoxic T lymphocytes (**CTLs**) kill targets through rapid release of perforin/granzymes into the lytic synapse. Lethal hit delivery activates programmed cell death in the target, which is classically considered apoptotic, caspase-mediated, and granzyme-dependent. Herein, we propose an unprecedented role for perforin in triggering target cell pyroptosis, complementing its well-documented role as a conduit for granzymes. Utilizing imaging and molecular approaches, we demonstrate that target perforation upon CTL attack elicits swift K^+ efflux, triggering the canonical inflammatory pyroptotic signaling cascade defined by activation of the NLRP3 inflammasome, caspase-1, and the pore-forming pyroptotic executioner, gasdermin D (**GSDMD**); this is followed by pyroptotic body formation, plasma membrane rupture, and release of intracellular contents. Disruption of perforin inhibited this pathway, while recombinant perforin activated caspase-1-dependent pyroptosis. These results reveal that perforin retains the pro-pyroptotic activity of ancestral pore-forming toxins, and highlight a previously unappreciated role for the canonical caspase-1/GSDMD pyroptotic pathway in adaptive immunity.

INTRODUCTION

$CD8^+$ cytotoxic T lymphocytes (CTLs) are potent, sensitive antigen-specific effector cells, which eliminate target cells upon recognition of cognate antigen. The most rapid of mechanism of cytotoxicity is the perforin/granzyme pathway, which involves directional secretion of cytotoxic molecules within specialized regions at the CTL-target cell interface termed lytic synapses (**LS**). Upon LS formation, the kinetics of attack and defense are extremely rapid[1]. Within seconds of lytic granule release, perforation of the target cell membrane by the pore-forming toxin perforin occurs; this facilitates delivery of granzymes, cytotoxic proteases that cleave intracellular substrates and engage the target cell's caspase network to promote programmed cell death (**PCD**)[2]. Target perforation also triggers Ca^{2+}-influx into the target cell, which can activate ultra-rapid Ca^{2+}-dependent reparative mechanisms at the LS (including lysosomal and ESCRT-mediated membrane repair)[3-5] that attenuate CTL-mediated cytotoxicity. Thus, the LS provides the spatiotemporal context within which pro-survival and pro-death pathways interact and compete to determine target cell fate.

The rapid activation of target cell caspases following CTL attack reinforced the longstanding paradigm that the perforin/granzyme pathway triggers target cell **apoptosis**[6-9], a slow, highly controlled, immunologically quiet cell death modality characterized by widespread intracellular caspase-mediated proteolysis and retention of plasma membrane integrity[10,11]. Broadly speaking, activation of the caspase network upon exposure to pro-apoptotic stimuli is responsible for the set of morphological and molecular features classically associated with apoptosis, such as phosphatidylserine (**PS**) externalization and formation of apoptotic bodies; such features typically appear within several hours of exposure to apoptotic stimuli, with cell death typically occurring over a more prolonged period of 8-20hr[11,12]. The morphology and kinetics of apoptosis contrast

strongly with the various forms of **programmed necrosis**, a collection of non-apoptotic programmed cell death modalities that includes pyroptosis and necroptosis among others[10,12]. These lytic cell death modalities are characterized by certain morphological features that collectively distinguish them from apoptosis, including the rapid uptake of vital dyes, plasma membrane rupture, and release of proinflammatory intracellular contents[10,12].

Although apoptosis was classically considered the main mediator of CTL-mediated target cell death, inflammatory, immunogenic and non-apoptotic cell death modalities have also been observed upon CTL attack[13-17]. Of particular interest is the highly inflammatory cell death modality known as **pyroptosis** ("fiery death"), which is frequently (though not exclusively) dependent upon activation of inflammatory or executioner caspases[18-21]. As a type of programmed necrosis, pyroptosis is characterized by rapid permeabilization of the plasma membrane, cell swelling/ballooning, plasma membrane rupture, and release of proinflammatory alarmins into the microenvironment, which triggers immune sentinel cell activation (reviewed in [12,22,23]). Because of its proinflammatory nature, pyroptosis is of tremendous interest in immuno-oncology, wherein it has been identified as a way to turn "cold" tumors "hot"; cell death modality is now considered an important functional determinant of antitumor immunity, treatment efficacy, and side effect profile[19,24].

The relatively recent discovery of pyroptosis prompted re-examination of the paradigm that target cells die by apoptosis upon CTL attack, and indeed several studies have provided evidence to support a pyroptotic cell death modality[25-27]. These findings called into question a fundamental pillar of CTL biology, prompting a re-examination of CTL-mediated killing and igniting a contentious debate regarding the mechanism and consequences of target cell death. In the context of immunotherapy, such findings are of tremendous importance, since identifying the cell death

pathways engaged upon CTL attack is important to help identify tumor cell defensive mechanisms, characterize the impact of cell death on the tumor microenvironment, and ultimately design combination therapies to promote tumor clearance while avoiding inflammatory side effects.

At the molecular level, pyroptosis is initiated by proteases (such as caspases) and executed by the gasdermin family of pore-forming proteins (GSDMA-E), which are expressed to varying degrees in transformed and untransformed cells[18,28]. Full-length gasdermins localize to the cytoplasm until proteolytic activation, which releases their pore-forming N-terminal domains[18,28,29]. Different gasdermins are cleaved by different proteases[18]; for instance, GSDME is a substrate of caspase-3, formerly considered a uniquely apoptotic caspase[19,26,27].

The first gasdermin to be identified in the context of pyroptosis was GSDMD[20,21,30-33], a quintessential mediator of innate immunity that is cleaved and activated by caspase-1 family proteases[30,34]. In the well-characterized "canonical" pyroptotic pathway, one or more inflammasomes (e.g. NLRP1, NLRP3) are activated as a result of intracellular homeostatic disruption, such as detection of pathogen-associated or damage-associated molecular patterns[35]; once assembled, inflammasomes mediate proximity-induced auto-activation of caspase-1, which in turn is responsible for the cleavage and activation of GSDMD. Cleaved GSDMD translocates to the plasma membrane, where it oligomerizes and forms stable pores[36,37]. GSDMD pores are impermeable to large molecules such as lactate dehydrogenase (**LDH)**[38] but selectively permeable to positively charged ions and small non-acidic proteins (e.g. mature interleukin (IL)-1β)[22,28,39,40]. In cells with highly functional membrane repair mechanisms, GSDMD pores can be removed, rendering pyroptosis reversible at early stages[41-44]. Otherwise, loss of membrane integrity leads to a collapse in electrochemical gradients, driving an influx of water through GSDMD pores[38,45]. This causes a characteristic "necrotic" cell death morphology[12], characterized by cell bloating/swelling

and formation of pyroptotic bodies, bubbling membrane protrusions that swell and contract stochastically in response to changing intracellular osmotic conditions[22,31,46]. Late-stage pyroptosis typically involves catastrophic membrane rupture, which releases proinflammatory alarmins (e.g. high mobility group box 1, **HMGB1**) and large cytoplasmic molecules (e.g. LDH) into the microenvironment. Although other pyroptotic pathways have since been identified (reviewed in [18,22,47]), the canonical NLRP3/caspase-1/GSDMD pathway remains a widely recognized and crucial pillar of innate immunity.

In the present study, we utilize imaging and molecular approaches to test the hypothesis that human antigen-specific CTLs induce this canonical pyroptotic signaling pathway in transformed target cells. Using live-cell imaging, we visualize rapid morphological changes consistent with pyroptosis following CTL attack, including cell swelling and pyroptotic body formation. We provide unprecedented evidence that the pyroptosis-initiating signal originates at the LS, whereupon perforin-mediated pore formation leads to K^+ efflux and activation of the canonical NLRP3/caspase-1/GSDMD pathway. To functionally position this pathway within the context of known mechanisms of CTL-mediated killing, we demonstrate that caspase-1 is engaged in parallel to caspase-3 (a primary activator of GSDME), and show that GSDMD/E double-knockdown reduces specific killing, even in the context of robust caspase-1 and caspase-3 activation. Collectively these results provide compelling evidence for a proinflammatory caspase-1/GSDMD pyroptotic signaling cascade upon perforin-mediated target perforation, and highlight a previously unappreciated role for perforin in target cell pyroptosis.

RESULTS

Target cell death upon attack by human Ag-specific CTL is characterized by membrane bubbling and loss of membrane integrity

To investigate target cell death upon CTL attack, we utilized a system wherein clonal antigen-specific human CTLs are conjugated with JY cells (an Epstein Barr virus (EBV)-transformed human B cell line used as a conventional target for human CTLs[48]), which had been pulsed or not with 10μM cognate antigen (peptide from human cytomegalovirus protein pp65); this well-characterized system enables us to focus upon the target cell response to CTL attack, in the context of strong antigenic stimulation and optimal CTL activation as previously described[3,4,49,50]. As JY cells are known to be highly sensitive to CTL attack[3,4,49], this cellular model provides an ideal framework for investigating lethal CTL:target cell interactions.

We first utilized time-lapse microscopy to visualize CTL-mediated target cell death, using low-concentration (6.6 μg/mL) propidium iodide (**PI**) as a vital dye. Consistent with previous results[3,4,49], non-antigen-pulsed target cells displayed transient non-lethal interactions with CTLs; only occasional cells become PI^+ within the 120min imaging period (**Supplemental Figure 1a,d**). By contrast, antigen-pulsed JY cells readily formed conjugates with CTLs, and of these, 78% became PI^+ within 120min (**Supplementary Figure 1b**). These observations confirmed the utility of this model system for studying lethal CTL-target interactions and provided an experimental framework within which to study the morphology of individual target cells upon CTL attack. Although this approach alone does not distinguish amongst the various types of programmed necrosis (pyroptosis, necroptosis, etc.), time-lapse microscopy remains a powerful and pragmatic approach for identifying the quintessential morphological features of non-apoptotic programmed cell death modalities (such as swelling, membrane bubbling, plasma membrane rupture, and vital

dye uptake)[12], which can be particularly informative when interpreted in combination with more specific molecular indicators (as described later).

As shown in **Figure 1**, CTL-mediated target cell death indeed bore several defining morphological characteristics which are shared by pyroptosis and other necrotic cell death modalities. In the example shown in **Figure 1a**, CTL cognate interaction with the target was indicated by Ca^{2+} flux and polarization of the CTL's microtubule organizing centre (**MTOC**) towards the LS (**Figure 1a** and **Supplementary Movie 1**). Rapidly thereafter, the target displayed irregular bubbling membrane protrusions, which expanded and contracted in the stochastic, erratic manner typical of pyroptotic bodies[22,31]. This bubbling was followed by cessation of cellular motility, bloating of the target, and ultimately explosive plasma membrane rupture, concurrent with instantaneous PI influx, all of which are prototypical morphological signs of pyroptosis and other necrotic cell death modalities, rather than apoptosis[12]. These observations were recapitulated in the second example shown in **Figure 1b** (wherein PI influx was slightly more gradual) and **Supplementary Movie 2**, and additional examples from three independent experiments (**Supplementary Figure 1c**). Such morphological features closely recapitulated the bubbling, lytic phenotype of pyroptosis exemplified by the K^+ ionophore nigericin[51-53], shown in **Supplementary Figure 2a,d** and **Supplementary Movies 3-5**), but contrasted starkly with the morphology of apoptosis (exemplified by the broad-spectrum kinase inhibitor staurosporine[12], shown in **Supplementary Figure 2b,d** and **Supplementary Movies 6-9**), whereupon cell death was slow, controlled, and lacked evidence of swelling, bubbling, or plasma membrane rupture.

To assess cell death morphology in individual cells longitudinally, we utilized a semi-automated image-processing pipeline to analyze changes in target cell size and shape over time following CTL attack. Non-pulsed cells were analyzed as a control (**Supplementary Figure 3** and

Supplementary Movie 10) and revealed the mild rhythmic oscillations in size (cross-sectional area) and shape (aspect ratio) typical of a live target cell. By contrast, upon CTL attack, dying target cells exhibited sharp, erratic fluctuations in cross-sectional area and aspect ratio concurrent with initiation of membrane bubbling, both of which stabilized upon cessation of cell motility (**Supplementary Figure 4a-d** and **Supplementary Movies 11-12**). These bubbling membrane protrusions combined with cell bloating caused transient expansion of target cells, with representative example cells exceeding 160% of their original cross-sectional area (**Supplementary Figure 4b**). This phenotype closely resembled nigericin-induced pyroptosis, wherein cross-sectional area and aspect ratio varied dramatically within the bubbling phase before stabilization upon cessation of cell movement (**Supplementary Figure 5a-d** and **Supplementary Movies 4-5**), with representative cells swelling up to 200% of their initial cross-sectional area immediately before lysis (**Supplementary Figure 5d**). By contrast, staurosporine-exposed apoptotic cells' cross-sectional area and aspect ratio remained steady throughout the imaging period (**Supplementary Figure 6a-d** and **Supplementary Movies 8-9**). Collectively, these results indicated that dying target cells exhibited a morphology that was consistent with pyroptosis (and other forms of programmed necrosis) following CTL attack.

Target cell death upon attack by human Ag-specific CTL is lytic and inflammatory

To determine whether CTL-mediated cell death also exhibited a molecular profile consistent with non-apoptotic cell death modalities, antigen-specific CTLs were conjugated with antigen-pulsed or non-pulsed target cells, subjected to Annexin V/PI assays and assessed by flow cytometry (gating strategy in **Supplementary Figure 7**). The Annexin V/PI assay is a highly sensitive and well-validated assay designed to distinguish both between early and late apoptosis, and between apoptosis and programmed necrosis[12]. It is based upon the premise that FITC-conjugated Annexin

V binds to externalized PS on the outer membrane of apoptotic cells, prior to the loss of membrane integrity and uptake of vital dyes; thus, when combined with PI as a vital dye, the Annexin V/PI assay permits discrimination between live cells (double negative), early-stage apoptotic cells (Annexin V single-positive), and end-stage apoptotic or necrotic cells (Annexin V/PI double-positive)[12]. Necrotic cell death modalities (including pyroptosis) do not accumulate a sizeable Annexin V single-positive population, and instead shift directly from double-negative to double-positive populations[12]. Of note, under prolonged *in vitro* conditions wherein phagocytic clearance of apoptotic cells cannot occur, end-stage apoptotic cells tend to undergo a process of secondary necrosis (example shown in **Supplemental Figure 2d**), leading to the uptake of vital dyes and the eventual accumulation of an AnnexinV/PI double-positive population[12]. As such, the double-positive population is not a distinguishing feature between programmed necrosis and late apoptosis; the important distinguishing feature in apoptosis is the presence of an Annexin V single-positive population, which is absent during pyroptosis and other forms of necrotic programmed cell death.

As shown in **Figure 1c-d**, Annexin V/PI double-positive target cells accumulated in a time-dependent fashion after 1hr and 4hr conjugation, but the Annexin V single-positive population remained unchanged across all time points, consistent with a non-apoptotic cell death mechanism. This closely recapitulated the phenotype of nigericin-exposed pyroptotic cells, which likewise acquired a substantial double-positive population and failed to accumulate an Annexin V single-positive population (**Supplementary Figure 8a,b**). By contrast, a significant increase in the Annexin V single-positive population was observed following staurosporine exposure (**Supplementary Figure 8a,b**), a classical feature of apoptosis that is notably absent upon CTL attack. Of note, the population of staurosporine-treated cells also contained a sizeable number of

Annexin V/PI double-positive (secondary necrotic) cells, which is quite typical of end-stage apoptosis *in vitro*[12].

To assess whether CTL-mediated cell death was associated with release of lytic or inflammatory molecules, supernatants were collected following conjugation of non-pulsed or antigen-pulsed target cells with CTLs for 1 or 4hr. As illustrated in **Figure 1e**, the classical alarmin and immunogenic cell death (**ICD**) marker HMGB1 was readily detectable in supernatant after 1hr. Likewise, supernatant LDH activity was readily detectable after 4hr conjugation (**Figure 1f**), consistent with a lytic cell death modality such as pyroptosis.

Collectively, these experiments indicated that target cell death upon CTL attack possessed the defining morphological features and molecular profile shared by pyroptosis and other lytic cell death modalities, including rapid expansion and contraction of pyroptotic bodies, stochastic changes in cell size and shape, loss of membrane integrity indicated by Annexin V/PI double-positivity, lack of an Annexin V-single positive population, and overt membrane lysis indicated by supernatant HMGB1 and LDH activity.

Target cell death is dependent upon the perforin pathway

We next sought to determine whether programmed necrosis upon CTL attack required the perforin secretory pathway by pre-treating CTLs with the well-established carboxylic ionophore monensin to increase lytic granule pH as well-described previously[3,4,54]. Interfering with the pH of lytic granules has been shown to markedly attenuate the efficacy of the perforin-mediated toxicity[3,55]. As shown in **Figure 1g**, target cells conjugated with monensin-treated CTLs failed to accumulate an Annexin V/PI double-positive population, suggesting that programmed necrosis was perforin-mediated.

In a complementary approach, we took advantage of the well-documented natural depletion of intracellular perforin stores following prolonged interactions between targets and cytotoxic lymphocytes[50,56-58]. It is known for both CTLs and NK cells that ultra-rapid perforin/granzyme-mediated killing ultimately gives way to slower complementary killing mechanisms such as death-receptor ligation, which is known to drive apoptosis[56-58]. Thus, we hypothesized that apoptotic target cells may be detectable following longer conjugations during which perforin is naturally depleted. To address this, cell death modality was assessed following overnight conjugations at both low (1:4) and high (4:1) E:T ratios, whereupon a sizeable apoptotic subpopulation of Annexin V single-positive target cells was indeed detectable (**Supplementary Figure 9a,b**), despite being largely absent from the target cell population at earlier timepoints (**Figure 1c,d**). This suggests that while the initial wave of perforin-dependent CTL-mediated cell death is lytic and inflammatory, apoptotic cell death mechanisms may come into play over time as lytic content becomes depleted.

Target cells express pyroptotic machinery at the transcript and protein level

Building upon the observation that initial perforin-dependent killing is lytic and inflammatory, we next sought to elucidate whether pyroptosis might be activated by target cell perforation. We first assessed transcript expression of *GSDMA-E* at baseline in JY cells and a diverse panel of other target cells. As shown in **Supplementary Figure 10a**, *GSDMD* and *GSDME* were the most highly and consistently expressed at baseline across a range of target cells. Given that GSDME has already been shown to have a role in target cell death upon attack by CTLs[26,27], we wanted to investigate the novel hypothesis that GSDMD may play a previously unidentified role in target cell pyroptosis upon CTL attack.

We next assessed whether GSDMD was expressed at the protein level in two well-characterized target cell lines: JY (described above) and D10, a well-characterized melanoma cell line,

moderately resistant to CTL attack due to membrane reparative turnover[3,4,59]. MDA-MB231 (a triple-negative breast cancer cell line, previously shown to highly express GSDMD[60] and GSDME[61]) was used as a positive control. Consistent with transcript data, full-length GSDMD protein was detectable in all three cell lines at baseline (**Supplementary Figure 10b**). Specificity of the GSDMD antibody was validated using siRNA approaches, wherein GSDMD signal was strongly reduced in *GSDMD*-targeting siRNA-transfected but not *GSDME*-targeting siRNA-transfected cells (**Supplementary Figure 10c,d**).

We next verified that both JY and D10 target cells could functionally undergo GSDMD-mediated pyroptosis upon short-term exposure to nigericin, which as described above induces canonical (NLRP3/caspase-1/GSDMD-dependent) pyroptosis[51-53]. After 2hr exposure to nigericin, the Annexin V/PI double positive population was significantly increased relative to solvent controls for both JY and D10 cells (**Supplementary Figure 11a,f**), while the Annexin V single-positive population remained unchanged for both cell lines (**Supplementary Figure 11b,g**). Substantial caspase-1 activity (as detected using a membrane-permeable activity-dependent caspase-1 probe) was detectable in nigericin-exposed cells within the 2hr time frame (**Supplementary Figure 11c,h**), which was accompanied by the detection of supernatant HMGB1 (**Supplementary Figure 11 d,i**) and LDH activity (**Supplementary Figure 11e,j**). Collectively, these results indicated that JY and D10 cells were both capable of undergoing canonical pyroptosis.

Cleaved GSDMD accumulates in target cells upon attack by CTLs and is enriched near the immunological synapse

Since JY cells are highly susceptible to CTL attack and capable of undergoing GSDMD-mediated pyroptosis in response to a pharmacological stimulus, we extended our studies in these cells and assessed whether cleaved GSDMD was detectable upon CTL attack. GSDMD has been proposed

to have a role in anti-tumor immunity[62] but its activation in the context of CTL attack has never been demonstrated. To accomplish this, we profited from two commercially available and widely utilized antibodies[63-66]: the first specifically detects the active N-terminal of GSDMD ("cleaved GSDMD") but not full-length GSDMD; and the second (also utilized for immunoblots above) detects both full-length and cleaved GSDMD ("total GSDMD"). JY cells were conjugated with CTLs for 15min, fixed, permeabilized, and stained with antibodies against cleaved GSDMD, total GSDMD, and perforin before being subjected to confocal microscopy. As shown in the illustrative 3D reconstruction in **Figure 2a**, total but not cleaved GSDMD immunoreactivity is detectable in non-pulsed target cells interacting with CTLs; however, upon interaction of pulsed JY cells with CTLs and initiation of target cell death, target cells display a high degree of cleaved GSDMD immunoreactivity, frequently associated with the bubbling morphology typical of pyroptosis. To facilitate quantification of cleaved GSDMD immunoreactivity in target cells upon CTL attack, we focused upon CTL- target cell conjugates where lytic granules were polarized towards the target but the target was still in the pre-bubbling stage. As shown in **Figure 2b,c**, while total GSDMD immunoreactivity was equivalent in both non-pulsed and pulsed target cells interacting with CTLs, cleaved GSDMD MFI significantly increased in targets under pulsed conditions after 15min conjugation. As a control, we showed that JY cells transfected with siRNA targeting *GSDMD* exhibited significantly reduced fluorescent signal from the cleaved GSDMD antibody (**Supplementary Figure 12a,b**).

Upon examination of cleaved GSDMD immunoreactivity in pulsed target cells upon CTL attack (**Figure 2b**), it became apparent that while total GSDMD was evenly distributed throughout the target cell, cleaved GSDMD immunoreactivity appeared concentrated near the LS in a subset of pulsed target cells, suggesting that the initial signal to activate GSDMD may first be triggered

locally near the LS. To quantify this observation, we assessed both cleaved and total GSDMD MFI in the synaptic half versus the distal half of pulsed target cells in conjugates with CTLs and generated a ratio of synaptic MFI /distal MFI; in this analysis, a ratio >1 indicated synaptic enrichment of the protein of interest, a ratio = 1 indicated even distribution throughout the cell. As shown in **Supplementary Figure 13**, after 15min conjugation, total GSDMD was evenly distributed throughout target cells in conjugation with CTLs under non-pulsed and pulsed conditions, but cleaved GSDMD (which was only consistently detectable under pulsed conditions) was frequently enriched on the synaptic side of the target cell. To determine whether this phenomenon might occur even more dramatically immediately after CTL attack, we performed the same analysis after only 5 min conjugation. As shown in **Figure 2e-g,** cleaved GSDMD was significantly enriched in target cells upon CTL attack even at this earlier time point. Under these conditions, cleaved GSDMD was strongly enriched near the LS while total GSDMD was evenly distributed throughout the cell (**Figure 2h,i**).

Caspase-1 activity is detectable in target cells upon CTL attack and is perforin-dependent

We next sought to test the hypothesis that caspase-1, the canonical caspase responsible for GSDMD activation, was activated in target cells upon CTL attack. To accomplish this, we first verified full-length caspase-1 expression at baseline in JY and D10 target cells, again using MDA-MB231 as a positive control (**Supplementary Figure 10e**). To test whether caspase-1 became activated specifically in targets upon CTL attack, we conjugated pulsed or non-pulsed JY cells with CTLs for 5 and 15min, after which conjugates were disrupted and subjected to flow cytometry analysis using a well-validated cell-permeable activity-dependent probe that irreversibly binds to active caspase-1 through covalent coupling[67,68]. This sensitive approach enabled the cell-type-specific quantification of caspase-1 activity in a mixed-cell system (gating strategy shown in

Supplementary Figure 14a). In the context of CTL attack, we demonstrated that the percentage of JY cells with caspase-1 activity rapidly increased following either a 5min or 15min CTL conjugation, compared to non-pulsed cells (**Figure 3a**). To validate the specificity of our read-out, we transfected JY cells with either non-targeting or *CASP1*-targeting siRNA (validation shown in **Supplementary Figure 10f**) and demonstrated that the fold-increase in caspase-1 probe activity in pulsed versus non-pulsed controls was decreased in the *CASP1* siRNA-transfected condition compared to non-targeting controls (**Supplementary Figure 14b**).

We next tested whether caspase-1 activation was antigen-dose dependent. Target cells were pulsed with different concentrations of peptide (from 1nM to 10μm) and conjugated with CTLs for 15 min; a significant increase in the percentage of cells with caspase-1 activity was observed with as little as 1nM antigenic peptide (**Figure 3b**). We performed a similar analysis to assess the effect of E:T ratio, wherein cells were pulsed with 10μm of antigen and subsequently conjugated with CTLs at an E:T ratio of 0.25, 1, or 4. As shown in **Figure 3c**, the percentage of cells with caspase-1 activity increased proportionally with E:T ratio, with an E:T ratio as low as 0.25 resulting in detectable caspase-1 activity after 15min conjugation.

Although many different types of inflammasomes have been identified, the NLRP3 inflammasome was of specific interest in this study since it is well-known to be activated by pore-forming toxins[69-74]. To test whether NLRP3 was involved in caspase-1 activation upon CTL attack, we first verified protein expression of NLRP3 in our target cells of interest (**Supplementary Figure 10e**) before assessing whether NLRP3 deficiency significantly affected caspase-1 activity following CTL attack in sensitive JY target cells. We compared the fold increase in caspase-1 MFI in JY targets transfected with either non-coding or *NLRP3*-targeting siRNA (validation shown in **Supplementary Figure 10f**) and conjugated with CTLs for 15min; this analysis revealed a small

but significant decrease in caspase-1 MFI when NLRP3 was knocked down compared to non-targeting controls (**Figure 3d**). The modest nature of this decrease is not unexpected considering that there are alternative inflammasomes that can be engaged under stress conditions to process caspase-1 (e.g. NLRP1, which detects abnormal protease activity and may also be sensitive to K^+ concentration[75,76] and NLRC4, which has been shown to be activated alongside NLRP3 in response to bacterial pore forming toxins[71]). Nonetheless, these data suggest a role for the NLRP3 inflammasome in this pyroptotic signaling axis.

Since we hypothesized that pore formation was a key initiating event in inflammasome activation, we next sought to determine whether the perforin/granzyme pathway was required to activate caspase-1/GSDMD through the use of monensin as described above. Herein, we pre-treated CTLs with monensin prior to conjugation with pulsed or non-pulsed targets; as shown in **Figure 3e**, monensin pre-treatment of CTLs largely abrogated caspase-1 activity, supporting the interpretation that the perforin/granzyme pathway is needed for caspase-1 activation.

Potassium flux is observed in target cells upon perforation by CTLs

K^+ efflux is considered an important activating signal for NLRP3 inflammasome activation[69,77-79] (reviewed in [80]). Since the insertion of pore-forming toxins (including aerolysin[70], *C. perfringens* β-toxin[81], *S. aureus*-derived PVL[73], *T. pyogenes*-derived pyolysin[74]) into the plasma membrane commonly leads to K^+ efflux[82], we hypothesized that perforin pore formation may likewise trigger immediate disruption of K^+ homeostasis in target cells upon CTL attack, providing an activating signal to NLRP3 (and potentially other K^+-sensitive inflammasomes). Although perforin pores are known to be selectively permeable to cationic cargo[83], direct assessment of K^+ loss upon target perforation by CTLs is largely absent from the literature. To address this, we made use of the well-described cell membrane-permeable fluorescent K^+ indicator, Ion Potassium Green-AM (IPG-AM;

formerly Asante Potassium Green-AM, APG-AM[84]), which has been widely used to assess intracellular K^+ concentration using both imaging and flow cytometry approaches[85-87]. Prior to assessing K^+ concentration in target cells upon CTL attack, we validated our flow cytometry approach using nigericin, whose primary mechanism of action is the reduction of intracellular K^+ concentration through K^+/H^+ exchange[32,51,52], and which has been previously validated using APG-AM probes[86]. As shown in **Supplementary Figure 15**, IPG-AM fluorescent signal decreases dramatically in a time-dependent manner upon exposure of JY cells to nigericin.

To assess changes in K^+ concentration upon CTL attack, non-pulsed and pulsed target cells were stained with IPG-AM, conjugated with CTLs for 5 or 15min at various E:T ratios, and subjected to analysis by flow cytometry. As shown in **Figure 4a-d**, a rapid E:T ratio-dependent loss of intracellular K^+ is observed in pulsed target cells upon conjugation with CTLs; the majority of K^+ efflux occurs rapidly upon CTL attack (ie within the first 5min of conjugation). This is consistent with the kinetics of caspase-1 activation (shown in **Figure 3a**) whereupon significant caspase-1 activity is also observed within 5min of CTL conjugation; this supports the notion that K^+ efflux upon target cell perforation provides the instigating signal for rapid caspase-1 processing. Importantly, dead cells are excluded from this analysis, which demonstrates that these K^+-low cells are indeed live cells that have diminished intracellular K^+.

Recombinant human perforin is sufficient to engage pyroptotic signaling pathways

To determine whether perforin was sufficient to initiate a pyroptotic signaling cascade in the absence of cytotoxic granzymes, we first exposed JY cells to recombinant human perforin in the presence of high-concentration PI (25μg/mL) to assess membrane perforation as previously reported[4]. As shown in **Figure 5a**, a dose-dependent perforation of JY cells was confirmed after incubation of JY cells with recombinant human perforin.

We next assessed whether such conditions were sufficient to induce K^+ efflux in target cells. As expected, a rapid and dose-dependent loss of intracellular K^+ was observed in JY cells upon exposure to recombinant human perforin, at 5 and 15min, based on loss IPG-AM signal (**Figure 5b** and **Supplemental Figure 16a,b**). To illustrate that this loss of signal was specific to loss of K^+ and not merely leakage of IPG-2 AM out of cells, a parallel set of experiments was conducted in which perforin was applied to JY cells in the presence of excess extracellular K^+, conditions under which the flow of K^+ ions out of the perforated cell would be effectively inhibited[69,76,79]. As shown in **Supplementary Figure 17b**, excess extracellular K^+ did in fact inhibit the loss of intracellular IPG-2 AM signal from perforated cells, despite not changing the perforating ability of perforin (**Supplementary Figure 17a**). These results confirm that the loss of IPG-2 AM signal in perforin-exposed cells is indeed attributable to K^+ efflux.

We then sought to test whether caspase-1 was activated downstream of perforation. As shown in **Figure 5c**, treatment with exogenous perforin significantly increased the percentage of cells with detectable caspase-1 activity. However, in parallel experiments performed in high K^+ buffer to prevent K^+ efflux, caspase-1 activity in perforin-exposed cells was reduced (**Figure 5d**) and the percentage of cells displaying caspase-1 activation was not significantly different than untreated controls (**Figure 5e**). Collectively, these data support a model wherein perforin-mediated pore formation leads to swift K^+ efflux from perforated cells, leading to activation of the canonical caspase-1 pathway.

Lastly, we assessed whether longer incubations of JY cells with recombinant perforin could trigger overt pyroptotic cell death. To assess this, we exposed JY cells to recombinant perforin for 60min and assessed cell death utilizing the Annexin V/PI assay. Consistent with a pyroptotic cell death modality, perforin exposure resulted in a significant increase in Annexin V/PI double-positive cells

(**Figure 5f**) but no increase in Annexin V single-positive cells. Moreover, no increase in PI single-positive cells was apparent, which argued against overt (non-programmed) necrotic cell death occurring from perforin-induced osmotic shock. Unlike pyroptosis, non-programmed necrotic phenomena such as osmotic shock cannot be prevented or delayed through pharmacological or genetic intervention[10]; to further illustrate that perforin-mediated cell death was programmed rather than overtly necrotic, we pre-treated JY cells with the caspase-1 inhibitor VX-765[64,88,89] (a well-validated, highly specific and cell-permeable peptidomimetic caspase-1 inhibitor). Compared to solvent-treated controls, cells that were pre-treated with VX-765 showed a significant reduction in perforin-induced cell death (**Figure 5g**), illustrating that recombinant perforin induced caspase-1-dependent programmed cell death.

Collectively, the experiments in this manuscript thus far have demonstrated a novel pyroptotic pathway that is activated upon perforation of the target cell, involving K^+ efflux, NLRP3 inflammasome activation, caspase-1 activity and ultimately GSDMD activation. With this insight, we next sought to functionally position this canonical caspase-1/GSDMD pathway within the context of known mechanisms of CTL-mediated killing.

Caspase-1 and -3 promote target cell pyroptosis through the GSDMD and GSDME pyroptotic pathways

Since our JY cells express both GSDMD and GSDME (**Supplementary Figure 10**), we hypothesized that these two pyroptotic pathways may serve as redundant mechanisms to drive target cell pyroptosis upon CTL attack. Caspase-3 is the major initiator of GSDME-mediated pyroptosis in cells that express GSDME, and is known to be robustly activated upon CTL attack[9,26,27,90]. As such, we first assessed activation of caspase-3 under parallel conditions as caspase-1, utilizing a caspase-3-specific cell-permeable activity-dependent fluorescent probe. These experiments demonstrated a significant time-dependent and antigen dose-dependent

activation of caspase-3 following 5 and 15min conjugation of target cells with CTLs (**Figure 6a,b**), which paralleled our observations with caspase-1. As little as 1nM of antigenic stimulation was sufficient to induce significant caspase-3 activity when pulsed cells were conjugated with CTLs (**Figure 6b**). We then conducted double-staining experiments to determine whether caspase-1 and caspase-3 activity were detectable in the same cells (**Figure 6c**). These experiments revealed a significant caspase-1 single-positive population, along with a robust double-positive population at both time points tested; caspase-3 single-positive cells remained relatively rare. Collectively, these data suggest that the two caspases are indeed frequently (but not exclusively) activated in the same cells upon CTL attack.

GSDMD and GSDME knockdown reduces CTL-mediated cytotoxicity

We next sought to establish whether concurrent inhibition of the two pyroptotic pathways would have a measurable effect on target cell death upon CTL attack. As such, we transfected JY cells with either non-targeting siRNA or a combination of both *GSDMD*- and *GSDME*-targeting siRNAs; knockdowns were validated by immunoblot (**Supplementary Figure 10c**). Transfected target cells were pulsed or not with antigenic peptide and conjugated with CTLs for 4hr before being subjected to Annexin V/PI analysis, while supernatants were collected for LDH assay. As shown in **Figure 6d**, concurrent knockdown of both pyroptotic pathways significantly inhibited the accumulation of Annexin V/PI double-positive cells, compared to the non-targeting siRNA condition; no increase in Annexin V single-positive cells was observed within this time frame, indicating that the inhibition of *GSDMD* and *GSDME* did not lead to a compensatory increase in apoptosis. Inhibition of both genes did however lead to a significant decrease in supernatant LDH activity (**Figure 6e**) in pulsed conditions. As expected, knockdown of *GSDMD* and *GSDME* did not affect the activation of their respective upstream caspases upon CTL attack (**Figure 6f,g**). This

provided the crucial piece of insight that even when executioner caspases are fully activated in target cells upon CTL attack, those target cells do not die as efficiently without the pyroptotic executioners GSDMD and GSDME as caspase substrates.

Melanoma cells activate the canonical pyroptosis signaling cascade upon CTL attack, which is increased through inhibition of reparative membrane turnover

We next utilized the D10 melanoma cell line described earlier, which is more resistant to CTL attack than JY cells due to enhanced reparative membrane turnover that promotes target cell survival even when facing fully activated CTLs[3,4,49,59]. In particular, melanoma cells are known to engage Ca^{2+}-dependent resistance mechanisms, including enhanced exposure of lysosomes at the lytic synapse, which enhances cathepsin-mediated perforin degradation and inhibits granzyme uptake into the target cell[3,4]. Although some melanoma target cell death occurs upon CTL attack even with intact membrane repair mechanisms, inhibition of Ca^{2+}-dependent repair through pre-treatment of melanoma cells with the Ca^{2+} chelator BAPTA-AM prior to conjugation with CTLs significantly increases target cell death upon conjugation with antigen-specific CTLs[3]. Nonetheless, the cell death modality which is engaged upon CTL attack (both at baseline and once Ca^{2+}-dependent membrane repair mechanisms are inhibited) is unknown.

To first examine whether cleaved GSDMD is detectable in D10 cells upon CTL attack, we conjugated pulsed or non-pulsed D10 cells with antigen-specific CTLs for 15 or 30min. As shown in the 3D re-construction in **Figure 7a**, cleaved GSDMD immunoreactivity was indeed detectable in dying D10 cells. Nonetheless, accumulation of cleaved GSDMD was delayed compared to JY cells, and was only detectable after 30min conjugation (**Figure 7b, c**) compared to JY cells in which cleaved GSDMD was detected after 5 and 15min (**Figure 2**).

We also observed that Annexin V/PI double-positive D10 cells accumulate after conjugation with CTLs for 1hr and 4hr (**Figure 7d**), but this occurs in a more limited fashion than JY cells under the same conditions as expected (**Figure 1**). Unlike JY cells, an Annexin V single-positive subpopulation (indicative of apoptotic cell death) was occasionally detectable at 1hr (**Figure 7d**). Nonetheless, increased LDH activity was observed in the supernatant after 4hr conjugation of pulsed D10 cells with CTLs, indicating that some lytic cell death did occur (**Figure 7e**). Crucially, caspase-1 activity was readily detectable in a subset of D10 cells following CTL attack, but in a more limited fashion than JY cells, after 5 and 15min conjugation (**Figure 7f**).

All of these results are consistent with a system wherein the previously described membrane repair mechanisms engaged rapidly upon CTL attack delay but do not entirely prevent target cell pyroptosis. To test this concept, we sought to determine whether inhibition of this membrane repair response as previously described[3] increased activation of pyroptosis-associated caspases. We pre-treated melanoma cells with the Ca^{2+} chelator BAPTA, which inhibits Ca^{2+}-dependent reparative membrane turnover and increases D10 cell death compared to solvent-treated controls[3]. Consistent with the hypothesis that inhibition of membrane reparative turnover increases pyroptotic signaling, we demonstrated that caspase-1 activity in pulsed D10 cells was significantly increased upon inhibition of Ca^{2+}-dependent reparative membrane turnover (**Figure 7g**).

DISCUSSION

In this manuscript, we describe for the first time the engagement of the canonical (caspase-1/GSDMD) pyroptotic signaling cascade in transformed target cells upon CTL attack, which is initiated at the LS by perforin-mediated pore formation (**Supplementary Figure 17**). This report not only supports previous studies that postulated a role for pyroptosis upon CTL attack[25-27], but also offers a novel mechanism for the engagement of pyroptotic machinery downstream of

perforin-mediated pore formation and supports a previously unknown role for GSDMD in CTL-mediated cell death. Conceptually, the pathway we identified links two different perforation events which cooperate to promote target cell death: the initial perforation of target cells by CTL-derived perforin (which is spatially constrained to the LS and temporally constrained by ultra-rapid synaptic membrane repair mechanisms[3-5]) followed by a more global perforation of target cells by their own endogenous pore-forming gasdermin proteins, which ultimately drives target cell death.

Importantly, this discovery ascribes a novel pro-pyroptotic function to perforin, alongside its classical role as a conduit for granzymes. The idea that perforin pore formation can activate the NLRP3/caspase-1/GSDMD pathway is consistent with a well-developed body of literature showing that cytotoxic pore-forming toxins, including *Aeromonas hydrophila* -derived aerolysin[69,70], *Vibrio pyarahaemolyticus*-derived thermostable direct hemolysins (TDH)[71], *Staphylococcus aureus*-derived Paton-Valentine leukocidin (PVL)[73], *Trueperella pyogenes*-derived pyolysin (PLO)[74] and *S. aureus*-derived α-hemolysin[69,72], trigger caspase-1 activation in perforated cells via the NLRP3 inflammasome. These bacterial pore-forming toxins are almost universally permeable to K^+ (reviewed in[82]), and not surprisingly, NLRP3/caspase-1 activation is often K^+ efflux-dependent[69-74]. Thus, perforin functionally mimics the activity of the ancestral pore-forming bacterial toxins described above, demonstrating that this ancient attack mechanism retains utility in the human CTL arsenal today. This ancestral mechanism may be useful to help CTLs circumvent granzyme-specific resistance mechanisms, such as the serine protease inhibitors (serpins), which have been shown to confer resistance to both chimeric antigen receptor (CAR) T cells and immune checkpoint blockade (ICB) therapy[91-93]. As such, engineering immunotherapies that potentiate perforin-activated pyroptotic signaling pathways may be a useful complementary approach.

We and others have shown that ultra-rapid Ca^{2+}-dependent membrane repair is a vital resistance mechanism against CTL attack[3-5]. Our current data implies that K^+ -dependent pro-death signalling may be initiated by the same perforation event as Ca^{2+}-dependent pro-survival repair mechanisms. Our previous studies have shown that BAPTA-AM-mediated inhibition of Ca^{2+}-dependent synaptic membrane repair results in an overt increase in target cell death[3], and the current study suggests that promotion of caspase-1-dependent pyroptosis may be one mechanism by which this occurs. Importantly, Ca^{2+}-dependent membrane repair mechanisms also facilitate the removal of gasdermin pores from the plasma membrane[41,42], and thus inhibition of membrane repair might be a doubly effective strategy for promoting both effective target perforation by perforin and ultimately gasdermin-mediated cell death.

Of note, Ca^{2+} flux has also been proposed as a common mediator of NLRP3 inflammasome activation[80,94], but in this study, chelation of intracellular Ca^{2+} with BAPTA-AM in D10 melanoma cells increased caspase-1 activation, suggesting that inflammasome activation in this system is not dependent on Ca^{2+} flux.

As mentioned above, the effect of siRNA-mediated NLRP3 inhibition on caspase-1 activity was modest in this system, and this observation is consistent with the presence of multiple other inflammasomes which may promote caspase-1 activation upon CTL attack[35]. Concurrent activation of other inflammasome sensors in combination with NLRP3 is well-documented (reviewed in [94]) and NLRC4 in particular has been shown to be activated alongside NLRP3 upon membrane perforation by bacterial pore forming toxins[71]. Likewise, NLRP1 can be activated upon disruption of intracellular K^+ homeostasis[76] and may serve as an additional platform for caspase-1 activation in our system. In addition to detecting loss of intracellular K^+, inflammasome sensors also collectively detect a diverse array of danger signals (including abnormal protease activity,

abnormal localization of nucleic acids, mitochondrial dysfunction, ROS production, disruption of the actin cytoskeleton, ribotoxic stress, and others)[35]. Many of these intracellular danger signals are present upon CTL attack[95], which may firstly ensure robust and continuous caspase-1 activation in the presence of continued danger and secondly make the activation of caspase-1 relatively robust to the depletion of an individual inflammasome sensor (such as NLRP3). Nonetheless, the results of our study align with a previous report that showed that antigen-dependent CTL feedback can induce NLRP3-dependent caspase-1 activation in antigen-presenting cells (APCs) through a perforin-dependent and K^+-dependent mechanism, although these interactions were non-lethal and instead led to sustained IL-1β secretion by viable APCs[96].

In this study, we provide evidence that caspase-1 is activated upon CTL attack, as well as upon exposure of target cells to recombinant human perforin (**Figure 2** and **5**). In addition to promoting GSDMD-mediated pyroptosis, caspase-1 activation may have additional downstream consequences; proteomics studies have revealed dozens of substrates for caspase-1, including cytoskeletal proteins, chaperone proteins (including heat shock proteins), and trafficking proteins (such as RAB7), as well as a notable constellation of proteins involved in glycolysis[34,97]. Although GSDMD is thought to be cleaved the fastest[34], this does not preclude a role for other caspase-1 substrates in the target cell response to CTL attack, which may become particularly relevant in the context of prolonged or sublethal encounters. Further studies will be necessary to elucidate other functions of caspase-1 prior to induction of CTL-driven pyroptosis.

Building upon previous studies of GSDME-mediated pyroptosis upon CTL attack[26,27], we also provide evidence in this study that concurrent inhibition of both GSDMD and GSDME diminishes specific killing upon CTL attack, despite robust caspase-1 and -3 activation (**Figure 6**). This suggests that caspase-1 and -3 activity alone is insufficient to achieve fast, optimal

perforin/granzyme-mediated cytotoxicity and supports a role for gasdermins as the final executioners of target cell death. The multi-pronged approach we propose (**Supplementary Figure 17**) in which both GSDMD and GSDME are activated upon CTL attack would be particularly important in transformed cells wherein individual gasdermins can be functionally inhibited through repression, inactivation, or mutation (reviewed in [47,95,98]). Thus, activation of multiple pyroptotic pathways upon CTL attack would increase the probability of successfully circumventing such resistance mechanisms. The evolution of multiple gasdermins has been speculated to serve precisely this purpose, offering multiple redundant or partially redundant cell death pathways that are activated during cellular stress[18]. More globally, the initiation of pyroptotic signaling pathways may serve as a "second blade" that can kill transformed cells wherein apoptotic pathways are inhibited.

Typically, plasma membrane permeabilization during pyroptosis is considered the main mechanisms of gasdermin-mediated toxicity; however, gasdermins have been shown to target other organelles enriched in cardiolipins, including lysosomes and mitochondria[62,99], causing mitochondrial depolarization, disruption of the mitochondrial network, release of mtDNA and mitochondrial proteins, and lysosome deacidification/decay, which ultimately lead to a failure of cell viability prior to PMR[62,100] (reviewed in [39]). Although we observed PMR in target cells in our system using live-cell imaging (**Figure 1**), the extent to which intracellular gasdermin-mediated injures contribute to target cell demise prior to lysis remains to be characterized.

Despite the aforementioned publications demonstrating roles for GSDME and GSDMB in CTL-mediated pyroptosis[25-27], the notion that CTL attack activates pyroptosis remains controversial within the field. Historically, apoptosis was the only well-recognized form of RCD in the literature and thus the notion that CTLs killed by apoptosis became a well-established paradigm. In this

study, we provide evidence for activation of caspase-1/GSDMD upon CTL attack and demonstrate that cytotoxicity of antigen-specific human CTLs is functionally diminished through siRNA-mediated inhibition of GSDMD and GSDME expression in targets, providing proof of principle that target cells are capable of dying by pyroptosis under the conditions of this study. Although these results do not suggest that the majority of CTL-driven cytotoxicity events across all species, diseases, and contexts is pyroptotic in nature, they do provide ample rationale for considering pyroptosis as a viable alternative mechanism for perforin/granzyme-mediated target cell death. Our results are consistent not only with the recent studies directly implicating pyroptosis in perforin/granyzme-mediated killing[25-27], but also with a number of earlier studies that highlighted non-apoptotic and/or immunogenic cell death modalities upon CTL attack[13-17]. Collectively, these studies involve a number of different contexts, across both mouse and human model systems, *in vitro* and *in vivo*, illustrating that our experimental conditions are not unique in promoting pyroptotic cell death upon CTL attack.

Further to this, it is worth emphasizing that cell death modality upon CTL attack is almost certainly context-dependent. On the CTL side, it is well-established that even clonal CTLs are phenotypically and functionally heterogeneous[101,102], and as such it stands to reason that CTL-intrinsic factors play a role in determining target cell death modality. Further live-cell imaging studies could reveal at the single-cell level whether individual CTLs preferentially induce a specific cell death modality, or whether individual CTLs trigger different cell death modalities as a result of different cytotoxic mechanisms engaged sequentially during serial killing (as has been proposed for NK cells[58], reviewed herein[103]). Furthermore, the newly identified supra-molecular attack particles (SMAPs)[104] may kill through different mechanisms than the classical perforin/granzyme

pathway, and as such the relative abundance of SMAPs in a given CTL population may impact its killing modality.

On the target cell side, cancer cells are highly heterogeneous, both at the intra-tumoral and inter-tumoral level, in terms of differentiation state, gene expression profile, mutational burden, presence or absence of viral genomic integration, epigenetic modifications, and ultimately functional behaviour[105]. This heterogeneity, particularly as it pertains to the dysregulation of cell death machinery, likely plays a large role in determining cell death modality. Dysregulation of apoptotic circuitry specifically was one of the six foundational hallmarks of cancer identified by Hanahan and Weinberg[106] and resistance to cell death through mutation, suppression, or dysreulgation of cell death machinery (both apoptotic and pyroptotic) continues to be considered a defining characteristic to the present day and major functional obstacle to CTL-mediated therapies[95,107,108]. The integration of viral genomes into cancer cells (particularly EBV, hepatitis B and human papilloma virus)[109] may introduce an additional level of cell death suppression through specific virally encoded modulators of cell death pathways. Thus, since an attacking CTL may face a transformed target wherein one or more cell death pathways have been rendered functionally impotent, the apoptosis-versus-pyroptosis decision balance must ultimately be influenced by which cell death pathways still retain a degree of functionality within the context of oncogenic transformation. Because multiple cell death pathways are initiated in parallel by an attacking CTL, it would not be unexpected that dying targets likewise display characteristics of multiple cell death modalities; some of these signaling pathways may be prematurely terminated due to the mutation, suppression, or inactivation of key components, while others may be actively involved in executing the cell death decision. For all of these reasons, cell death modality upon CTL attack is likely to be

context-dependent and may not fit neatly into a single well-described PCD modality due to the multi-pronged nature of CTL attack.

In the context of oncology, multiple chemotherapeutics[19,110,111], small molecule inhibitors[112], radiation[113-115], and tumor immunotherapy[25,27] as well as nanoparticle-based approaches for therapeutic delivery of gasdermins[41,116] have been shown to drive tumor cell pyroptosis, which strongly favours anti-tumor immunity and tumor clearance, particularly in the context of turning "cold" tumors "hot" (reviewed in [24,98]). Mass spectrometry-based human proteomics studies have revealed that GSDMD-mediated pyroptosis releases several hundred different proteins, through a combination of conventional secretion, unconventional secretion, vesicle/lysosome release, and passive cell lysis (e.g. LDH)[23]. The pyroptotic secretome is particularly enriched in DAMPs (e.g, HMGB1, galectins, S100 family proteins, and lysosomal cathepsins) which collectively serve as potent proinflammatory danger signals in the extracellular environment, through various mechanisms including direct TLR ligation[23]. Activation of local inflammatory signaling cascades by the pyroptotic secretome in turn leads to increased anti-tumor immunity by acting on multiple steps of the cancer-immunity cycle[117], including enhanced antigen presentation, priming of APCs, and immune infiltration, as reviewed elsewhere[24,98]. As such, our results fit within a mature field of literature that has repeatedly highlighted how pyroptotic tumor cell death can favour anti-tumor immunity.

However, pyroptosis is a double-edged sword, which has also been associated with tumorigenesis in certain contexts[98] as well as adverse inflammatory side effects including cytokine release syndrome[27,118] and certain side-effects of chemotherapeutics[19]. Since cell death modality is known to have such a profound impact on treatment efficacy and side effect profile, one can envision there would be clinical utility in delineating how given CTL-mediated immunotherapies induce cell

death. Given that expression of gasdermin family proteins is heterogeneous both within and between tumor types (reviewed in [47,98]), it is conceivable that individual tumors have a pre-existing "fingerprint" of gene expression which sensitizes them to different cell death modalities and may impact efficacy and side effect profile of CTL-mediated therapies. Depending upon whether it is clinically advisable to promote or inhibit inflammatory cell death, different combination therapies could be envisioned that are designed to enhance or prevent pyroptosis. Proof of concept for this has already been demonstrated with chemotherapeutics, wherein the methyltransferase inhibitor decitabine enhanced GSDME expression and promoted pyroptosis following nanoparticle-mediated delivery of cisplatin[110].

Outside the context of tumor immunology, understanding whether CTLs can trigger target cell pyroptosis may be crucially important for neuroinflammatory conditions (such as multiple sclerosis[64,119]), autoimmune disease, and chronic infection, wherein canonical GSDMD-dependent pyroptosis has been implicated as a driver of chronic inflammation[47,120,121]. In such conditions, the inflammatory pyroptotic secretome perpetuates bystander tissue damage, leading to a feed-forward cycle of tissue damage and inflammation[47,120]; as such, understanding and preventing CTL-driven pyroptosis may be a widely applicable therapeutic approach.

In conclusion, our study provides compelling evidence that ion flux at the LS triggers a novel proinflammatory caspase-1/GSDMD pyroptotic signaling cascade, which may prove to be an important consideration in the context of immuno-oncology and related fields. We propose a novel pro-pyroptotic function for perforin, which is consistent with the role of prokaryotic pore-forming toxins and expands its cytotoxic role beyond that of a simple conduit for granzymes.

METHODS

Cell Culture

Cell culture was performed as previously described[3,4]. Human $CD8^+$ T cells were purified from healthy donor blood samples using the RosetteSep Human $CD8^+$ T Cell Enrichment Cocktail (StemCell Technologies). For cloning, HLA-A2-restricted $CD8^+$ T cells specific for the NLVPMVATV peptide of the cytomegalovirus protein pp65 were single-cell sorted into 96-U-bottom plates using a BD FACSAria II cell sorter using tetramer staining. Cells were cultured in RPMI 1640 medium supplemented with 5% human AB serum (Inst. Biotechnologies J.BOY), 50µmol/L 2-mercaptoethanol, 10mM HEPES, 1X MEM NEAA (Gibco), 1X Sodium pyruvate (Sigma), 10µg/ml ciprofloxacine (AppliChem), 100 IU/ml human rIL-2 and 50 ng/ml human rIL-15 (Miltenyi). $CD8^+$ T-cell clones were stimulated in complete RPMI/HS medium containing 1 µg/ml PHA with 1 x 10^6 per ml 35 Gy irradiated allogeneic peripheral blood mononuclear cells (isolated on FicollPaque Gradient from blood of healthy donors). Clones were restimulated every 2 weeks. Blood samples were collected and processed following standard ethical procedures after obtaining written informed consent from each donor and approval by the French Ministry of Research (transfer agreement AC-2020-3971). Approbation by the ethical department of the French Ministry of the Research for the preparation and conservation of cell lines and clones starting from healthy donor human blood samples has been obtained (authorization no. DC-2021-4673).

EBV-transformed B cells (JY) HLA-$A2^+$ were used as sensitive target cells. D10 HLA-$A2^+$ human melanoma cell lines were isolated from melanoma patients and kindly provided by Dr G. Spagnoli, Basel, Switzerland. All target cells were cultured in RPMI 1640 GlutaMAX supplemented with 10% FCS and 50µmol/L 2-mercaptoethanol, 10mM HEPES, 1X MEM NEAA (Gibco), 1X Sodium pyruvate (Sigma), 10µg/ml ciprofloxacine (AppliChem). All cell lines were screened biweekly for

mycoplasma contamination using MycoAlert mycoplasma detection kit (Lonza). Melanoma and JY cells were subjected to cell line typing (Microsynth Ecogenics, Switzerland) to authenticate their identity and ensure that no contamination of human origin was detectable.

Drug treatments

To induce pyroptosis, cells were plated at a density of 2.5 x 10^4 cells per well in a 96-well plate, treated with 100μM nigericin (CliniSciences #ICT-6698 or Invivogen #tlrl-nig) and incubated at 37°C and 5% CO_2 for the indicated time (2hr unless otherwise indicated). This high concentration of nigericin was utilized to ensure that the majority of cells underwent swift and definitive pyroptosis and to circumvent the need for an LPS-priming step. To induce apoptosis, cells were plated using the same conditions and treated with 6.6μM staurosporine (*Streptomyces*) (InSolution, Merck #569396) and incubated at 37°C and 5% CO_2 for the indicated time.

To assess the effect of Ca^{2+} chelation in target cells on pyroptotic signaling pathways, target cells were treated with 50μM BAPTA-AM for 2hr at 37°C (ThermoFisher Scientific, #B6769) and thoroughly washed before conjugation with CTLs.

To test the effect of CTL lytic granule depletion, CTLs were pre-treated with monensin (FisherScientific GolgiStop™ containing 0.26% monensin, diluted 1:1000, #BDB554724) for 2hr at 37°C and thoroughly washed before conjugation with targets.

To assess the effects of caspase-1 inhibition, targets were pre-treated for 2hr with 100μM VX-765 (InvivoGen, #inh-vx765) during the 2hr antigen pulse step and washed prior to conjugation with CTLs.

Annexin V/PI Apoptosis Detection

Target cells (JY and D10) were either non-pulsed or pulsed with 10µM CMV p65 antigenic peptide for 2hr at 37°C and 5% CO_2, washed and transferred to a 96-well U-bottom plate at 1 x 10^4 cells per 100µl RPMI 5% FCS/HEPES. CTL were previously stained with CellTrace™ Violet (ThermoFisher Scientific, #C34557) for 30min at 37°C and 5% CO_2, washed and added to the target cells at an effector:target ratio of 4:1 in 100µl RPMI 5% FCS/HEPES. Plates containing samples were spun for 1min and incubated at 37°C and 5% CO_2 for either 1 or 4hr. At the endpoint, cells were spun, washed in ice cold PBS, and assayed for Annexin V and PI staining according to manufacturer's instructions (BD Pharmingen FITC Annexin V Apoptosis Detection Kit I, #AB_2869082). In a subset of experiments, CTLs were treated with monensin (BD GolgiStop™; #51-2092KZ) at a dilution of 1:1000 for 2hr and washed thoroughly prior to conjugation with targets. Samples were acquired using the MACSQuant Analyzer 10 flow cytometer (Miltenyi Biotec) and analyzed using FlowJo 10.

For drug controls, target cells were plated at a density of 2.5 x 10^4 cells per well in a 96-well U-bottom plate, incubated with either nigericin (pyroptosis control), staurosporine (apoptosis control), or solvent controls for the indicated time, and subjected to Annexin V and PI staining as described above.

Lactate Dehydrogenase Supernatant Activity Assay

Target cells (JY and D10) were either non-pulsed or pulsed with 10µM CMV p65 antigenic peptide for 2hr at 37°C and 5% CO_2, washed and transferred to a 96-well U-bottom plate at 1 x 10^4 cells per 100µl RPMI 5% FCS/HEPES. CTL were added to the target cells at an effector:target ratio of 4:1 in 100µl RPMI 5% FCS/HEPES. Plates containing samples were spun for 1min and incubated at 37°C and 5% CO_2 for 4hr. At the endpoint, cells were spun and supernatant removed for storage at -20°C and then analyzed using the CytoSelect™ LDH Cytotoxicity Assay Kit (Cell Biolabs Inc,

#CBA-241) according to manufacturer's instructions. Absorbance (optical density at 450nm) was assessed using a CLARIOstar plate reader (BMG Labtech).

As a positive control, JY and D10 target cells were plated at a density of 2.5 x 10^4 cells per well in a 96-well U-bottom plate and incubated with 100µM nigericin or solvent controls for 2hr. Supernatants were harvested and subjected to LDH detection as described above.

HMGB1 Immunoassay

Target cells (JY and D10) were either non-pulsed or pulsed with 10µM CMV p65 antigenic peptide for 2hr at 37°C and 5% CO_2, washed and transferred to a 96-well U-bottom plate at 2.5 x 10^4 cells per 100µl RPMI 5% FCS/HEPES. CTL were added to the target cells at an effector:target ratio of 4:1 in 100µl RPMI 5% FCS/HEPES. Plates containing samples were spun for 1min and incubated at 37°C and 5% CO_2 for 1hr. At the endpoint, supernatant was removed for immediate analysis using the LumitTM HMGB1 (Human/Mouse) Immunoassay (Promega, #W6110). Luminescent samples were read in opaque white 96-well plates using a CLARIOstar plate reader (BMG Labtech).

As a positive control, JY and D10 target cells were plated at a density of 2.5 x 10^4 cells per well in a 96-well U-bottom plate and incubated with 100µM nigericin or solvent controls for 2hr. Supernatants were harvested and subjected to HMGB1 assay as described above.

Caspase-1 and Caspase-3 Activity-Dependent Fluorescent Assays

Target cells were either non-pulsed or pulsed with 10µM CMV p65 antigenic peptide unless otherwise indicated for 2hr at 37°C and 5% CO_2, washed and transferred to a 96-well U-bottom plate at 1 x 10^4 cells per 100µl RPMI 5% FCS/HEPES. Plated target cells were single-or double-stained with either far-red fluorescence FLICA 660 Caspase-1 (YVAD) reagent

(ImmunoChemsitry, #9122) or green fluorescent FAM-FLICA Caspase-3/7 (DEVD) reagent (ImmunoChemsitry, #93), according to manufacturer's instructions for 20min at 37°C and 5% CO_2. CTL were stained with CellTrace™ Violet (ThermoFisher Scientific, #C34557) for 30min at 37°C and 5% CO_2, washed and added to the target cells at an effector:target ratio of 4:1 unless otherwise indicated in 100µl RPMI 5% FCS/HEPES. Plates containing samples were spun for 1min and incubated at 37°C and 5% CO_2 for either 5 or 15min. At the endpoint, cells were washed, fixed with the provided fixative (ImmunoChemistry #636), and stored at 4°C before being acquired using the MACSQuant Analyzer 10 flow cytometer (Miltenyi Biotec) and analyzed using FlowJo 10. In a subset of experiments, CTLs were treated with monensin (BD GolgiStop™; #51-2092KZ) at a dilution of 1:1000 for 2hr and washed thoroughly prior to conjugation with targets.

As a positive control, JY and D10 target cells were plated at a density of 2.5 x 10^4 cells per well in a 96-well U-bottom plate and incubated with 100µM nigericin or solvent controls for 2hr, before being stained with FLICA 660 Caspase-1 (YVAD) reagent for 20 mins and analyzed as described above.

Transfection of Target Cells

From 8 x 10^5 to 1x 10^6 JY cells were washed and resuspended in 100µl OPTI-MEM and transferred in electroporation cuvettes (0.2cm). 200 pmoles of each different siRNA targeting mRNA coding for *GSDMD*, *GSDME*, *CASP1*, *NLRP3*, or non-targeting siRNA were added in the cell suspension. After electroporation at 160V during 10 ms (500µF) with a exponential waveform using the Gene PulserXcell Electroporation systems (Bio-rad), transfected JY cells were seeded in pre-warmed culture medium and used for experiments 24-48h after electroporation. Transfection efficiency was evaluated by qPCR or immunoblot.

Target	siRNA Sequence (5'->3')
GSDMD	s36339 : GGAACUCGCUAUCCCUGUUtt s36340 : CGUGAGUGUGGACCCUAAtt s36341 : AGCUGGUUAUUGACUCUGAtt
GSDME	S230618 : GAGAGAACAAUAAAUCUGAtt S4065 : GGAUGGACCAUUAAGUGUUtt S4066 : GAAAGAUACAGAAAGGUUUtt
NLRP3	s41554 : GGAGAGACCUUUAUGAGAAtt s41555 : GCUUUGUCCUCGGUACUCAtt s41556 : GCACGUGUUUCGAAUCCCAtt
CASP1	s2407 : GGAAGACUCAUUGAACAUAtt s2408 : CCACUGAAAGAGUGACUUUtt s2409 : UGGAGGAAAUUUUCCGCAAtt
Non-targeting	4390843 (proprietary sequence) 4390846 (proprietary sequence)

Potassium Efflux Assays

To assess the relative intracellular concentration of K^+ upon target cell perforation, JY cells were non-pulsed or pulsed with 10μM antigenic peptide (CMV p65) for 2hr at 37° and 5% CO_2, washed, and loaded with 2.5 μM Ion Potassium Green-2 AM (Abcam, ab142806) for 30min. Stained JY cells were then conjugated with antigen-specific CTLs at the indicated effector:target ratios for 5 and 15min, stained with viability dye (eFluor 450) and subjected to analysis by flow cytometry. Samples were acquired using the MACSQuant Analyzer 10 or MACS Quant Analyzer VYB flow cytometers (Miltenyi Biotec) and analyzed using FlowJo 10.

As a positive control, JY cells were plated in 96-well U-bottom plates at a density of 2.5 x 10^4 cells/well and treated with the K^+ ionphore nigericin (100μM) at time points ranging from 1min to 2hr, before being stained with IPG-2 AM and viability dye and analyzed as above.

Exogenous Perforin Experiments

To assess target cell perforation by recombinant perforin, JY target cells were plated in 96-well U-bottom plates at a density of 2.5 x 10^4 cells/well in perforin binding buffer to facilitate perforin

phospholipid binding (20mM HEPES, 150nM NaCl, 2.5mM $CaCl_2$) containing PI (25µg/mL). Recombinant human perforin-1 (AA 22-555, Enzo Life Science ENZ-PRT313-0200) was added at the indicated concentrations for a duration of 15min, after which cells were spun, washed, and re-suspended for analysis by flow cytometry. In experiments with excess extracellular K^+, the perforin binding buffer above was replaced with buffer containing KCl)20mM HEPES, 150nM NaCl, 2.5mM $CaCl_2$).

To assess intracellular K^+ concentration, JY cells were plated in 96-well U-bottom plates at a density of 2.5 x 10^4 cells/well in perforin binding buffer and stained with the fluorescent K^+ probe, Ion Potassium Green-2 AM for 30min as described above. Recombinant perforin was added at a concentration of 4 or 8µg/mL for 5 and 15min, after which cells were spun, washed and analyzed by flow cytometry.

To assess caspase-1 activation, JY cells were plated in 96-well U-bottom plates at a density of 2.5 x 10^4 cells/well in perforin binding buffer and pre-loaded with far-red caspase-1 activity-dependent probe (ImmunoChemsitry, #9122). Recombinant perforin was added at a concentration of 8µg/mL for 30min, after which cells were spun, washed, and fixed with the provided fixative (ImmunoChemistry #636), prior to analysis by flow cytometry.

For Annexin V/PI assays, JY cells were plated in 96-well U-bottom plates at a density of 2.5 x 10^4 cells/well in perforin binding buffer and recombinant perforin added at a concentration of 8µg/mL for 60min, after which cells were washed and subjected to Annexin V/PI staining as described above (BD Pharmingen FITC Annexin V Apoptosis Detection Kit I, #AB_2869082) before analysis by flow cytometry.

Real-time quantitative PCR

Isolation of RNA was performed using the Quick-RNA mini Prep kit (ZymoResearch) and RNA concentration was assessed with the NanoDrop 1000 system (Thermo Scientific). cDNA was synthesized using the SuperScript™ IV VILO™ (SSIV VILO) Master Mix (Invitrogen).

The gene expression of *GSDMA-E*, *CASP1* and *NLRP3* was evaluated by real-time quantitative (RTqPCR) using TaqMan gene expression assays (Applied Biosystems) according to manufacturer's recommendations, using a StepOne Real-Time PCR System (Applied Biosysrems). All reactions were performed in triplicates and relative gene expression levels were evaluated using the comparative CT (threshold cycle) method (2-deltaCT). GAPDH was used as endogenous controls for normalization.

Target	Sequence
GSDMA	Hs00403267_m1
GSDMB	Hs00218565_m1
GSDMC	Hs00937071_m1
GSDMD	Hs00986748_g1
GSDME	Hs00903185_m1
NLRP3	Hs00918082_m1
CASP1	Hs00354836_m1
GAPDH	Hs99999905_m1

Immunoblot

Sample collection: To assess baseline expression of pyroptosis proteins (GSDMD, GSDME, NLRP3 and caspase-1), 2.5 x 10^6 JY, D10, or MDA-MB231 cells were washed in cold PBS and resuspended in RIPA buffer with cOmplete™ protease inhibitor cocktail (Sigma-Aldrich).

Protein extraction and immunoblot: After 15min on ice with agitation every 5min, extracts were centrifuged to pellet DNA and the supernatant was collected. Proteins were quantified by Pierce BCA protein assay kit (Thermo Fisher Scientific) according to manufacturer's instructions. Proteins were then denatured in Laemli buffer (5min at 95° with agitation). 15µg of protein was loaded for each sample in precast 4-15% Mini-Protean TGX Stain-Free 30µl 10-well polyacrylamide gels (Bio-Rad #456803) along with Kaleidoscop protein ladder (Bio-Rad). Gels were run and blotted onto a nitrocellulose membrane and blocked with 3% non-fat dry milk in Tris-buffered saline with Tween (TBST) for 1hr. Membrane was incubated with the indicated primary antibodies overnight at 4°C with agitation, followed by 1hr incubation with the corresponding HRP-tagged secondary antibodies. Blots were developed using ECL Clarity (Max) detection reagent (Bio-Rad) and imaged using ChemiDoc MP System (Bio-Rad).

Primary Antibodies

Target	Application	Isotype	Supplier	Identifier	Dilution
GSDMD (*total*)	WB/IF	Mouse IgG1	Sigma	Clone 3F12-1B2 #WH0079792M1	WB: 1/200 IF: 1/100
GSDMD (*cleaved*)	IF	Rabbit mAb IgG	Cell Signaling	(Asp275) #36425	IF: 1/50
GSDME (*total*)	WB	IgG2A	Abnova	Clone 1E10 #H00001687-M01	WB: 1/1000
Caspase-1 (*total*)	WB	Mouse IgG2A	R&D Systems	Clone 661228 #MAB6215	WB: 1/5000
NLRP3	WB	Mouse IgG1	Novus Bio	CLO210, #NBP2-52879	WB: 1/500
Perforin	IF	Mouse IgG2B	BD	#556434	IF: 1/200
Beta-actin	WB	Mouse IgG2A	Sigma Aldrich	Clone AC-74 #A5316	1/5000

Secondary Antibodies

Name	Application	Supplier	Identifier	Concentration
Goat anti-Rabbit HRP	WB	Cell Signaling`	7074S	1/2500
Goat anti-Mouse IgG HRP	WB	Cell Signaling	7076S	1/2500
Goat anti-rabbit Alexa Fluor™ Plus 488	IF	Invitrogen	A32731	1/100
Goat anti-Mouse IgG2b Alexa Fluor™ 555	IF	Invitrogen	A21147	1/100
Goat anti-Mouse IgG1 Alexa Fluor™ 647	IF	Invitrogen	A21240	1/100

Immunofluorescence

JY target cells were either non-pulsed or pulsed with 10μM antigenic peptide (CMV p65) for 2hr at 37 °C and 5% CO_2 in RPMI 5% FCS/HEPES, washed three times, and conjugated at an effector:target ratio of 1:1 with antigen-specific human CTLs using 1 min centrifugation at 455g. Conjugates were incubated for 5 or 15 min, gently disrupted, and subsequently seeded on Poly-L-Lysine-coated slides. Cells were fixed with 3% paraformaldehyde at 37 °C for 10min. Cells were then permeabilized with 0.1% saponin (in PBS/3%BSA/HEPES), and stained with the indicated primary antibodies overnight at RT followed by isotype-matched secondary antibodies for 1hr at RT. Samples were washed, mounted in 90% glycerol-PBS containing 2.5% DABCO (Sigma) and examined using a LSM 880 (Zeiss) confocal microscope using a 63x objective. 3D images (using the z-stack function) were acquired at 1μm intervals.

To assess GSDMD expression in target cells, cells were manually outlined and the MFI of total and cleaved GSDMD within the target cell measured (using the Measure function of ImageJ) on 5 different planes of the *z*-stack (separated by 1μm) at the height of the IS and subsequently averaged. To ensure consistency in the quantification, only target cells in the pre-bubbling stage were included in the analysis, and cells with highly irregular bubbling protrusions or ruptured membranes were excluded.

To assess whether total and cleaved GSDMD were expressed evenly throughout the target cell or enriched proximal to the synapse, each target cell was divided into two halves in the x-y plane (synaptic and distal) and MFI quantified separately for each half of the cell. This analysis was repeated in both the cleaved and total GSDMD channels across 5 sequential planes of the z-stack at the height of the IS and the average ratio of synaptic:distal signal was calculated for each cell. According to this analysis, a synaptic:distal ratio greater than 1 indicates synaptic enrichment;

equal to 1 indicates even distribution of signal throughout the cell, and less than 1 indicates distal enrichment. For this analysis, the mean synaptic:distal ratio for each channel was compared to a hypothetical value of 1 (indicating even intracellular distribution) using a one-sample *t*-test.

Time Lapse Microscopy

For drug treatment experiments, JY cells were preloaded with CellMask™ Deep Red plasma membrane stain (1µg/mL) (Invitrogen, #C10046) for 30 min at 37°C with 5% CO_2, washed, and then seeded in RPMI 1640 medium with 10% FCS at 2 x 10^5 - 3 x 10^5 cells per well on poly-D-lysine coated 8-well chambered slides (Ibidi) for 5 min before imaging. Propidium iodide was added at a concentration of 6.6µg/mL. Drugs were added at the indicated concentrations: nigericin (100µM), staurosporine (6.7 µM), or solvent control. Timelaspe micrsocopy was performed within a temperature-controlled chamber using multi position acquisition (3 positions) overnight on a spinning-disk microscope. All time-lapse microscope experiments were acquired on a spinning disk microscope equipped with APO lbda 60X NA 1.4 objective. The temperature controlled chamber was maintained at 37°C and a constant 5% CO2 concentration. A Prime 95B Scientific sCMOS Camera (Photometrics) was used for acquisition. Image acquisition was controlled by MetaMorph Software (Molecular Devices 7.10.5.476) and by Modular V2.0 GATACA software.

To analyze the morphological features (cross-sectional area and aspect ratio) of dying target cells over the duration of the imaging period, target cell masks were generated using ImageJ software (version 1.53o), using the following semi-automated image processing pipeline: first, images were split into channels. Then, the variance filter was applied to the transmission channel (radius 5.0) followed by “Threshold” and “Transform to Binary”. Next, the “Erode” binary function option was applied and manually cross-checked against the transmission channel. Finally, the “Fill Holes”

function was applied and where possible, the “Add Mask” function was utilized to generate the outline. The “Watershed” function was applied as the final step and manual correction was performed as needed on a slice-by-slice basis to remove debris and artifacts. “Analyze Particle” was utilized to draw outlines after manual correction, after which a macro was used to generate the black background and white foreground, and to label and save the mask area. Thus, a cell mask was generated for each cell at every time-point throughout the imaging period, from which the cross-sectional area and aspect ratio could be calculated and plotted over time.

To visualize the morphological features of JY cells dying upon CTL attack, JY cells were pulsed with 10µM peptide, preloaded with Cell Mask DeepRed plasma membrane stain (1µg/mL) (Invitrogen), washed and seeded at 2.5 x 10^4 cells per wells on poly-D-lysine coated 16 wells-chambered slides (Ibidi). CTL clones were preloaded with Fluo-8-AM (0.25ng/µL) (AAT Bioquest) and SPY650 Tubulin (2X) (Spirochrome) or Tubulin Tracker Deep Red (2.56µg/µL) (Invitrogen) for 30min, washed and added at 4 x 10^4 to 5 x 10^5 cells per wells. Propidium iodide (6.6µg/mL) was added immediately before the acquisition. In these experiments, cells were kept in RPMI 1640 with 5% FCS medium for the imaging period.

For the analysis, the three channels were split (transmission, CellMask, Fluo-8-AM). Then, the variance filter was applied to the transmission channel (radius 5.0) and a binary option applied (manually cross-checked against the transmission image). In order to remove the CTL from analysis, the “Create Mask” function was applied to the Fluo-8-AM channel and subtracted from the selection (either the Brightfield/variance or CellMask Channel) using Image Calculator. Finally, the “Fill Holes” and “Watershed” functions were applied and adjusted manually as required. “Analyze Particle” was utilized as a final step described above.

REFERENCES

1 Wiedemann, A., Depoil, D., Faroudi, M. & Valitutti, S. Cytotoxic T lymphocytes kill multiple targets simultaneously via spatiotemporal uncoupling of lytic and stimulatory synapses. *Proc Natl Acad Sci U S A* **103**, 10985-10990, doi:10.1073/pnas.0600651103 (2006).

2 Lopez, J. A. *et al.* Perforin forms transient pores on the target cell plasma membrane to facilitate rapid access of granzymes during killer cell attack. *Blood* **121**, 2659-2668, doi:10.1182/blood-2012-07-446146 (2013).

3 Filali, L. *et al.* Ultrarapid lytic granule release from CTLs activates Ca(2+)-dependent synaptic resistance pathways in melanoma cells. *Sci Adv* **8**, eabk3234, doi:10.1126/sciadv.abk3234 (2022).

4 Khazen, R. *et al.* Melanoma cell lysosome secretory burst neutralizes the CTL-mediated cytotoxicity at the lytic synapse. *Nat Commun* **7**, 10823, doi:10.1038/ncomms10823 (2016).

5 Ritter, A. T. *et al.* ESCRT-mediated membrane repair protects tumor-derived cells against T cell attack. *Science* **376**, 377-382, doi:10.1126/science.abl3855 (2022).

6 Cullen, S. P. & Martin, S. J. Mechanisms of granule-dependent killing. *Cell Death Differ* **15**, 251-262, doi:10.1038/sj.cdd.4402244 (2008).

7 Weigelin, B. & Friedl, P. T cell-mediated additive cytotoxicity - death by multiple bullets. *Trends Cancer* **8**, 980-987, doi:10.1016/j.trecan.2022.07.007 (2022).

8 Barry, M. & Bleackley, R. C. Cytotoxic T lymphocytes: all roads lead to death. *Nat Rev Immunol* **2**, 401-409, doi:10.1038/nri819 (2002).

9 Adrain, C., Murphy, B. M. & Martin, S. J. Molecular ordering of the caspase activation cascade initiated by the cytotoxic T lymphocyte/natural killer (CTL/NK) protease granzyme B. *J Biol Chem* **280**, 4663-4673, doi:10.1074/jbc.M410915200 (2005).

10 Galluzzi, L. *et al.* Molecular mechanisms of cell death: recommendations of the Nomenclature Committee on Cell Death 2018. *Cell Death Differ* **25**, 486-541, doi:10.1038/s41418-017-0012-4 (2018).

11 Taylor, R. C., Cullen, S. P. & Martin, S. J. Apoptosis: controlled demolition at the cellular level. *Nat Rev Mol Cell Biol* **9**, 231-241, doi:10.1038/nrm2312 (2008).

12 Costigan, A., Hollville, E. & Martin, S. J. Discriminating Between Apoptosis, Necrosis, Necroptosis, and Ferroptosis by Microscopy and Flow Cytometry. *Curr Protoc* **3**, e951, doi:10.1002/cpz1.951 (2023).

13 Zychlinsky, A., Zheng, L. M., Liu, C. C. & Young, J. D. Cytolytic lymphocytes induce both apoptosis and necrosis in target cells. *J Immunol* **146**, 393-400 (1991).

14 Blanchard, D. K. *et al.* Role of extracellular adenosine triphosphate in the cytotoxic T-lymphocyte-mediated lysis of antigen presenting cells. *Blood* **85**, 3173-3182 (1995).

15 Waterhouse, N. J. *et al.* Cytotoxic T lymphocyte-induced killing in the absence of granzymes A and B is unique and distinct from both apoptosis and perforin-dependent lysis. *J Cell Biol* **173**, 133-144, doi:10.1083/jcb.200510072 (2006).

16 Jaime-Sanchez, P. *et al.* Cell death induced by cytotoxic CD8(+) T cells is immunogenic and primes caspase-3-dependent spread immunity against endogenous tumor antigens. *J Immunother Cancer* **8**, doi:10.1136/jitc-2020-000528 (2020).

17 Martinez-Lostao, L., Anel, A. & Pardo, J. How Do Cytotoxic Lymphocytes Kill Cancer Cells? *Clin Cancer Res* **21**, 5047-5056, doi:10.1158/1078-0432.CCR-15-0685 (2015).

18 De Schutter, E. *et al.* Punching Holes in Cellular Membranes: Biology and Evolution of Gasdermins. *Trends Cell Biol* **31**, 500-513, doi:10.1016/j.tcb.2021.03.004 (2021).

19 Wang, Y. *et al.* Chemotherapy drugs induce pyroptosis through caspase-3 cleavage of a gasdermin. *Nature* **547**, 99-103, doi:10.1038/nature22393 (2017).

20 Kayagaki, N. *et al.* Caspase-11 cleaves gasdermin D for non-canonical inflammasome signalling. *Nature* **526**, 666-671, doi:10.1038/nature15541 (2015).
21 Liu, X. *et al.* Inflammasome-activated gasdermin D causes pyroptosis by forming membrane pores. *Nature* **535**, 153-158, doi:10.1038/nature18629 (2016).
22 Yu, P. *et al.* Pyroptosis: mechanisms and diseases. *Signal Transduct Target Ther* **6**, 128, doi:10.1038/s41392-021-00507-5 (2021).
23 Phulphagar, K. *et al.* Proteomics reveals distinct mechanisms regulating the release of cytokines and alarmins during pyroptosis. *Cell Rep* **34**, 108826, doi:10.1016/j.celrep.2021.108826 (2021).
24 Zhang, Z., Zhang, Y. & Lieberman, J. Lighting a Fire: Can We Harness Pyroptosis to Ignite Antitumor Immunity? *Cancer Immunol Res* **9**, 2-7, doi:10.1158/2326-6066.CIR-20-0525 (2021).
25 Zhou, Z. *et al.* Granzyme A from cytotoxic lymphocytes cleaves GSDMB to trigger pyroptosis in target cells. *Science* **368**, doi:10.1126/science.aaz7548 (2020).
26 Zhang, Z. *et al.* Gasdermin E suppresses tumour growth by activating anti-tumour immunity. *Nature* **579**, 415-420, doi:10.1038/s41586-020-2071-9 (2020).
27 Liu, Y. *et al.* Gasdermin E-mediated target cell pyroptosis by CAR T cells triggers cytokine release syndrome. *Sci Immunol* **5**, doi:10.1126/sciimmunol.aax7969 (2020).
28 Ruhl, S. & Broz, P. Regulation of Lytic and Non-Lytic Functions of Gasdermin Pores. *J Mol Biol* **434**, 167246, doi:10.1016/j.jmb.2021.167246 (2022).
29 Krawczyk, P. A., Laub, M. & Kozik, P. To Kill But Not Be Killed: Controlling the Activity of Mammalian Pore-Forming Proteins. *Front Immunol* **11**, 601405, doi:10.3389/fimmu.2020.601405 (2020).
30 Sborgi, L. *et al.* GSDMD membrane pore formation constitutes the mechanism of pyroptotic cell death. *EMBO J* **35**, 1766-1778, doi:10.15252/embj.201694696 (2016).
31 Chen, X. *et al.* Pyroptosis is driven by non-selective gasdermin-D pore and its morphology is different from MLKL channel-mediated necroptosis. *Cell Res* **26**, 1007-1020, doi:10.1038/cr.2016.100 (2016).
32 Russo, H. M. *et al.* Active Caspase-1 Induces Plasma Membrane Pores That Precede Pyroptotic Lysis and Are Blocked by Lanthanides. *J Immunol* **197**, 1353-1367, doi:10.4049/jimmunol.1600699 (2016).
33 He, W. T. *et al.* Gasdermin D is an executor of pyroptosis and required for interleukin-1beta secretion. *Cell Res* **25**, 1285-1298, doi:10.1038/cr.2015.139 (2015).
34 Agard, N. J., Maltby, D. & Wells, J. A. Inflammatory stimuli regulate caspase substrate profiles. *Mol Cell Proteomics* **9**, 880-893, doi:10.1074/mcp.M900528-MCP200 (2010).
35 Barnett, K. C., Li, S., Liang, K. & Ting, J. P. A 360 degrees view of the inflammasome: Mechanisms of activation, cell death, and diseases. *Cell* **186**, 2288-2312, doi:10.1016/j.cell.2023.04.025 (2023).
36 Mulvihill, E. *et al.* Mechanism of membrane pore formation by human gasdermin-D. *EMBO J* **37**, doi:10.15252/embj.201798321 (2018).
37 Ding, J. *et al.* Pore-forming activity and structural autoinhibition of the gasdermin family. *Nature* **535**, 111-116, doi:10.1038/nature18590 (2016).
38 DiPeso, L., Ji, D. X., Vance, R. E. & Price, J. V. Cell death and cell lysis are separable events during pyroptosis. *Cell Death Discov* **3**, 17070, doi:10.1038/cddiscovery.2017.70 (2017).
39 Devant, P. & Kagan, J. C. Molecular mechanisms of gasdermin D pore-forming activity. *Nat Immunol* **24**, 1064-1075, doi:10.1038/s41590-023-01526-w (2023).
40 Xia, S. *et al.* Gasdermin D pore structure reveals preferential release of mature interleukin-1. *Nature* **593**, 607-611, doi:10.1038/s41586-021-03478-3 (2021).

41 Li, Z. *et al.* Enhancing Gasdermin-induced tumor pyroptosis through preventing ESCRT-dependent cell membrane repair augments antitumor immune response. *Nat Commun* **13**, 6321, doi:10.1038/s41467-022-34036-8 (2022).
42 Ruhl, S. *et al.* ESCRT-dependent membrane repair negatively regulates pyroptosis downstream of GSDMD activation. *Science* **362**, 956-960, doi:10.1126/science.aar7607 (2018).
43 Nozaki, K. *et al.* Caspase-7 activates ASM to repair gasdermin and perforin pores. *Nature* **606**, 960-967, doi:10.1038/s41586-022-04825-8 (2022).
44 Shkarina, K. *et al.* Optogenetic activators of apoptosis, necroptosis, and pyroptosis. *J Cell Biol* **221**, doi:10.1083/jcb.202109038 (2022).
45 Kovacs, S. B. & Miao, E. A. Gasdermins: Effectors of Pyroptosis. *Trends Cell Biol* **27**, 673-684, doi:10.1016/j.tcb.2017.05.005 (2017).
46 Zhang, Y., Chen, X., Gueydan, C. & Han, J. Plasma membrane changes during programmed cell deaths. *Cell Res* **28**, 9-21, doi:10.1038/cr.2017.133 (2018).
47 Liu, X., Xia, S., Zhang, Z., Wu, H. & Lieberman, J. Channelling inflammation: gasdermins in physiology and disease. *Nat Rev Drug Discov* **20**, 384-405, doi:10.1038/s41573-021-00154-z (2021).
48 Reiss, C. S. *et al.* Development and characterization of allospecific long-term human cytolytic T-cell lines. *Proc Natl Acad Sci U S A* **77**, 5432-5436, doi:10.1073/pnas.77.9.5432 (1980).
49 Caramalho, I., Faroudi, M., Padovan, E., Muller, S. & Valitutti, S. Visualizing CTL/melanoma cell interactions: multiple hits must be delivered for tumour cell annihilation. *J Cell Mol Med* **13**, 3834-3846, doi:10.1111/j.1582-4934.2008.00586.x (2009).
50 Faroudi, M. *et al.* Lytic versus stimulatory synapse in cytotoxic T lymphocyte/target cell interaction: manifestation of a dual activation threshold. *Proc Natl Acad Sci U S A* **100**, 14145-14150, doi:10.1073/pnas.2334336100 (2003).
51 Perregaux, D. & Gabel, C. A. Interleukin-1 beta maturation and release in response to ATP and nigericin. Evidence that potassium depletion mediated by these agents is a necessary and common feature of their activity. *J Biol Chem* **269**, 15195-15203 (1994).
52 Walev, I., Reske, K., Palmer, M., Valeva, A. & Bhakdi, S. Potassium-inhibited processing of IL-1 beta in human monocytes. *EMBO J* **14**, 1607-1614, doi:10.1002/j.1460-2075.1995.tb07149.x (1995).
53 Mariathasan, S. *et al.* Cryopyrin activates the inflammasome in response to toxins and ATP. *Nature* **440**, 228-232, doi:10.1038/nature04515 (2006).
54 Nakazato, K. & Hatano, Y. Monensin-mediated antiport of Na+ and H+ across liposome membrane. *Biochim Biophys Acta* **1064**, 103-110, doi:10.1016/0005-2736(91)90416-6 (1991).
55 Kataoka, T. *et al.* Concanamycin A, a powerful tool for characterization and estimation of contribution of perforin- and Fas-based lytic pathways in cell-mediated cytotoxicity. *J Immunol* **156**, 3678-3686 (1996).
56 Hassin, D., Garber, O. G., Meiraz, A., Schiffenbauer, Y. S. & Berke, G. Cytotoxic T lymphocyte perforin and Fas ligand working in concert even when Fas ligand lytic action is still not detectable. *Immunology* **133**, 190-196, doi:10.1111/j.1365-2567.2011.03426.x (2011).
57 Meiraz, A., Garber, O. G., Harari, S., Hassin, D. & Berke, G. Switch from perforin-expressing to perforin-deficient CD8(+) T cells accounts for two distinct types of effector cytotoxic T lymphocytes in vivo. *Immunology* **128**, 69-82, doi:10.1111/j.1365-2567.2009.03072.x (2009).
58 Prager, I. *et al.* NK cells switch from granzyme B to death receptor-mediated cytotoxicity during serial killing. *J Exp Med* **216**, 2113-2127, doi:10.1084/jem.20181454 (2019).
59 Khazen, R., Muller, S., Lafouresse, F., Valitutti, S. & Cussat-Blanc, S. Sequential adjustment of cytotoxic T lymphocyte densities improves efficacy in controlling tumor growth. *Sci Rep* **9**, 12308, doi:10.1038/s41598-019-48711-2 (2019).

60 Yan, H. *et al.* Cisplatin Induces Pyroptosis via Activation of MEG3/NLRP3/caspase-1/GSDMD Pathway in Triple-Negative Breast Cancer. *Int J Biol Sci* **17**, 2606-2621, doi:10.7150/ijbs.60292 (2021).
61 Zhang, Z. *et al.* Caspase-3-mediated GSDME induced Pyroptosis in breast cancer cells through the ROS/JNK signalling pathway. *J Cell Mol Med* **25**, 8159-8168, doi:10.1111/jcmm.16574 (2021).
62 Miao, R. *et al.* Gasdermin D permeabilization of mitochondrial inner and outer membranes accelerates and enhances pyroptosis. *Immunity* **56**, 2523-2541 e2528, doi:10.1016/j.immuni.2023.10.004 (2023).
63 McKenzie, B. A. *et al.* Activation of the executioner caspases-3 and -7 promotes microglial pyroptosis in models of multiple sclerosis. *J Neuroinflammation* **17**, 253, doi:10.1186/s12974-020-01902-5 (2020).
64 McKenzie, B. A. *et al.* Caspase-1 inhibition prevents glial inflammasome activation and pyroptosis in models of multiple sclerosis. *Proc Natl Acad Sci U S A* **115**, E6065-E6074, doi:10.1073/pnas.1722041115 (2018).
65 Megli, C., Morosky, S., Rajasundaram, D. & Coyne, C. B. Inflammasome signaling in human placental trophoblasts regulates immune defense against Listeria monocytogenes infection. *J Exp Med* **218**, doi:10.1084/jem.20200649 (2021).
66 Ma, H., Jeppesen, J. F. & Jaenisch, R. Human T Cells Expressing a CD19 CAR-T Receptor Provide Insights into Mechanisms of Human CD19-Positive beta Cell Destruction. *Cell Rep Med* **1**, 100097, doi:10.1016/j.xcrm.2020.100097 (2020).
67 Duhalde Vega, M. *et al.* PD-1/PD-L1 blockade abrogates a dysfunctional innate-adaptive immune axis in critical beta-coronavirus disease. *Sci Adv* **8**, eabn6545, doi:10.1126/sciadv.abn6545 (2022).
68 Clark, K. M. *et al.* Chemical inhibition of DPP9 sensitizes the CARD8 inflammasome in HIV-1-infected cells. *Nat Chem Biol* **19**, 431-439, doi:10.1038/s41589-022-01182-5 (2023).
69 Munoz-Planillo, R. *et al.* K(+) efflux is the common trigger of NLRP3 inflammasome activation by bacterial toxins and particulate matter. *Immunity* **38**, 1142-1153, doi:10.1016/j.immuni.2013.05.016 (2013).
70 Gurcel, L., Abrami, L., Girardin, S., Tschopp, J. & van der Goot, F. G. Caspase-1 activation of lipid metabolic pathways in response to bacterial pore-forming toxins promotes cell survival. *Cell* **126**, 1135-1145, doi:10.1016/j.cell.2006.07.033 (2006).
71 Higa, N. *et al.* Vibrio parahaemolyticus effector proteins suppress inflammasome activation by interfering with host autophagy signaling. *PLoS Pathog* **9**, e1003142, doi:10.1371/journal.ppat.1003142 (2013).
72 Craven, R. R. *et al.* Staphylococcus aureus alpha-hemolysin activates the NLRP3-inflammasome in human and mouse monocytic cells. *PLoS One* **4**, e7446, doi:10.1371/journal.pone.0007446 (2009).
73 Holzinger, D. *et al.* Staphylococcus aureus Panton-Valentine leukocidin induces an inflammatory response in human phagocytes via the NLRP3 inflammasome. *J Leukoc Biol* **92**, 1069-1081, doi:10.1189/jlb.0112014 (2012).
74 Liang, H., Wang, B., Wang, J., Ma, B. & Zhang, W. Pyolysin of Trueperella pyogenes Induces Pyroptosis and IL-1beta Release in Murine Macrophages Through Potassium/NLRP3/Caspase-1/Gasdermin D Pathway. *Front Immunol* **13**, 832458, doi:10.3389/fimmu.2022.832458 (2022).
75 Mitchell, P. S., Sandstrom, A. & Vance, R. E. The NLRP1 inflammasome: new mechanistic insights and unresolved mysteries. *Curr Opin Immunol* **60**, 37-45, doi:10.1016/j.coi.2019.04.015 (2019).
76 Rozario, P. *et al.* Mechanistic basis for potassium efflux-driven activation of the human NLRP1 inflammasome. *Proc Natl Acad Sci U S A* **121**, e2309579121, doi:10.1073/pnas.2309579121 (2024).

77 Petrilli, V. *et al.* Activation of the NALP3 inflammasome is triggered by low intracellular potassium concentration. *Cell Death Differ* **14**, 1583-1589, doi:10.1038/sj.cdd.4402195 (2007).
78 Fernandes-Alnemri, T. *et al.* The pyroptosome: a supramolecular assembly of ASC dimers mediating inflammatory cell death via caspase-1 activation. *Cell Death Differ* **14**, 1590-1604, doi:10.1038/sj.cdd.4402194 (2007).
79 Tapia-Abellan, A. *et al.* Sensing low intracellular potassium by NLRP3 results in a stable open structure that promotes inflammasome activation. *Sci Adv* **7**, eabf4468, doi:10.1126/sciadv.abf4468 (2021).
80 Gong, T., Yang, Y., Jin, T., Jiang, W. & Zhou, R. Orchestration of NLRP3 Inflammasome Activation by Ion Fluxes. *Trends Immunol* **39**, 393-406, doi:10.1016/j.it.2018.01.009 (2018).
81 Nagahama, M. *et al.* The p38 MAPK and JNK pathways protect host cells against Clostridium perfringens beta-toxin. *Infect Immun* **81**, 3703-3708, doi:10.1128/IAI.00579-13 (2013).
82 Dal Peraro, M. & van der Goot, F. G. Pore-forming toxins: ancient, but never really out of fashion. *Nat Rev Microbiol* **14**, 77-92, doi:10.1038/nrmicro.2015.3 (2016).
83 Stewart, S. E. *et al.* The perforin pore facilitates the delivery of cationic cargos. *J Biol Chem* **289**, 9172-9181, doi:10.1074/jbc.M113.544890 (2014).
84 Rana, P. S. *et al.* Calibration and characterization of intracellular Asante Potassium Green probes, APG-2 and APG-4. *Anal Biochem* **567**, 8-13, doi:10.1016/j.ab.2018.11.024 (2019).
85 Wong, F. *et al.* Cytoplasmic condensation induced by membrane damage is associated with antibiotic lethality. *Nat Commun* **12**, 2321, doi:10.1038/s41467-021-22485-6 (2021).
86 Camilli, G. *et al.* beta-Glucan-induced reprogramming of human macrophages inhibits NLRP3 inflammasome activation in cryopyrinopathies. *J Clin Invest* **130**, 4561-4573, doi:10.1172/JCI134778 (2020).
87 Ren, G. *et al.* ABRO1 promotes NLRP3 inflammasome activation through regulation of NLRP3 deubiquitination. *EMBO J* **38**, doi:10.15252/embj.2018100376 (2019).
88 Flores, J. *et al.* Caspase-1 inhibition alleviates cognitive impairment and neuropathology in an Alzheimer's disease mouse model. *Nat Commun* **9**, 3916, doi:10.1038/s41467-018-06449-x (2018).
89 Dhani, S., Zhao, Y. & Zhivotovsky, B. A long way to go: caspase inhibitors in clinical use. *Cell Death Dis* **12**, 949, doi:10.1038/s41419-021-04240-3 (2021).
90 Yang, X. *et al.* Granzyme B mimics apical caspases. Description of a unified pathway for trans-activation of executioner caspase-3 and -7. *J Biol Chem* **273**, 34278-34283, doi:10.1074/jbc.273.51.34278 (1998).
91 Li, X. *et al.* Apoptotic caspase-7 activation inhibits non-canonical pyroptosis by GSDMB cleavage. *Cell Death Differ* **30**, 2120-2134, doi:10.1038/s41418-023-01211-3 (2023).
92 Kimman, T. *et al.* Serpin B9 controls tumor cell killing by CAR T cells. *J Immunother Cancer* **11**, doi:10.1136/jitc-2022-006364 (2023).
93 Jiang, P. *et al.* Signatures of T cell dysfunction and exclusion predict cancer immunotherapy response. *Nat Med* **24**, 1550-1558, doi:10.1038/s41591-018-0136-1 (2018).
94 Swanson, K. V., Deng, M. & Ting, J. P. The NLRP3 inflammasome: molecular activation and regulation to therapeutics. *Nat Rev Immunol* **19**, 477-489, doi:10.1038/s41577-019-0165-0 (2019).
95 McKenzie, B., Khazen, R. & Valitutti, S. Greek Fire, Poison Arrows, and Scorpion Bombs: How Tumor Cells Defend Against the Siege Weapons of Cytotoxic T Lymphocytes. *Front Immunol* **13**, 894306, doi:10.3389/fimmu.2022.894306 (2022).
96 Yao, Y. *et al.* Antigen-specific CD8(+) T cell feedback activates NLRP3 inflammasome in antigen-presenting cells through perforin. *Nat Commun* **8**, 15402, doi:10.1038/ncomms15402 (2017).

97 Shao, W., Yeretssian, G., Doiron, K., Hussain, S. N. & Saleh, M. The caspase-1 digestome identifies the glycolysis pathway as a target during infection and septic shock. *J Biol Chem* **282**, 36321-36329, doi:10.1074/jbc.M708182200 (2007).
98 Loveless, R., Bloomquist, R. & Teng, Y. Pyroptosis at the forefront of anticancer immunity. *J Exp Clin Cancer Res* **40**, 264, doi:10.1186/s13046-021-02065-8 (2021).
99 Rogers, C. *et al.* Gasdermin pores permeabilize mitochondria to augment caspase-3 activation during apoptosis and inflammasome activation. *Nat Commun* **10**, 1689, doi:10.1038/s41467-019-09397-2 (2019).
100 de Vasconcelos, N. M., Van Opdenbosch, N., Van Gorp, H., Parthoens, E. & Lamkanfi, M. Single-cell analysis of pyroptosis dynamics reveals conserved GSDMD-mediated subcellular events that precede plasma membrane rupture. *Cell Death Differ* **26**, 146-161, doi:10.1038/s41418-018-0106-7 (2019).
101 Vasconcelos, Z. *et al.* Individual Human Cytotoxic T Lymphocytes Exhibit Intraclonal Heterogeneity during Sustained Killing. *Cell Rep* **11**, 1474-1485, doi:10.1016/j.celrep.2015.05.002 (2015).
102 Lemaitre, F., Moreau, H. D., Vedele, L. & Bousso, P. Phenotypic CD8+ T cell diversification occurs before, during, and after the first T cell division. *J Immunol* **191**, 1578-1585, doi:10.4049/jimmunol.1300424 (2013).
103 Ramirez-Labrada, A. *et al.* All About (NK Cell-Mediated) Death in Two Acts and an Unexpected Encore: Initiation, Execution and Activation of Adaptive Immunity. *Front Immunol* **13**, 896228, doi:10.3389/fimmu.2022.896228 (2022).
104 Balint, S. *et al.* Supramolecular attack particles are autonomous killing entities released from cytotoxic T cells. *Science* **368**, 897-901, doi:10.1126/science.aay9207 (2020).
105 Fisher, R., Pusztai, L. & Swanton, C. Cancer heterogeneity: implications for targeted therapeutics. *Br J Cancer* **108**, 479-485, doi:10.1038/bjc.2012.581 (2013).
106 Hanahan, D. & Weinberg, R. A. The hallmarks of cancer. *Cell* **100**, 57-70, doi:10.1016/s0092-8674(00)81683-9 (2000).
107 Hanahan, D. & Weinberg, R. A. Hallmarks of cancer: the next generation. *Cell* **144**, 646-674, doi:10.1016/j.cell.2011.02.013 (2011).
108 Hanahan, D. Hallmarks of Cancer: New Dimensions. *Cancer Discov* **12**, 31-46, doi:10.1158/2159-8290.CD-21-1059 (2022).
109 Zapatka, M. *et al.* The landscape of viral associations in human cancers. *Nat Genet* **52**, 320-330, doi:10.1038/s41588-019-0558-9 (2020).
110 Fan, J. X. *et al.* Epigenetics-Based Tumor Cells Pyroptosis for Enhancing the Immunological Effect of Chemotherapeutic Nanocarriers. *Nano Lett* **19**, 8049-8058, doi:10.1021/acs.nanolett.9b03245 (2019).
111 Erkes, D. A. *et al.* Mutant BRAF and MEK Inhibitors Regulate the Tumor Immune Microenvironment via Pyroptosis. *Cancer Discov* **10**, 254-269, doi:10.1158/2159-8290.CD-19-0672 (2020).
112 Lu, H. *et al.* Molecular Targeted Therapies Elicit Concurrent Apoptotic and GSDME-Dependent Pyroptotic Tumor Cell Death. *Clin Cancer Res* **24**, 6066-6077, doi:10.1158/1078-0432.CCR-18-1478 (2018).
113 Liu, Y. G. *et al.* NLRP3 inflammasome activation mediates radiation-induced pyroptosis in bone marrow-derived macrophages. *Cell Death Dis* **8**, e2579, doi:10.1038/cddis.2016.460 (2017).
114 Tan, G. *et al.* Radiosensitivity of colorectal cancer and radiation-induced gut damages are regulated by gasdermin E. *Cancer Lett* **529**, 1-10, doi:10.1016/j.canlet.2021.12.034 (2022).
115 Li, H. *et al.* Pyroptotic cell death: an emerging therapeutic opportunity for radiotherapy. *Cell Death Discov* **10**, 32, doi:10.1038/s41420-024-01802-0 (2024).

116 Wang, Q. *et al.* A bioorthogonal system reveals antitumour immune function of pyroptosis. *Nature* **579**, 421-426, doi:10.1038/s41586-020-2079-1 (2020).
117 Mellman, I., Chen, D. S., Powles, T. & Turley, S. J. The cancer-immunity cycle: Indication, genotype, and immunotype. *Immunity* **56**, 2188-2205, doi:10.1016/j.immuni.2023.09.011 (2023).
118 Deng, T., Tang, C., Zhang, G. & Wan, X. DAMPs released by pyroptotic cells as major contributors and therapeutic targets for CAR-T-related toxicities. *Cell Death Dis* **12**, 129, doi:10.1038/s41419-021-03428-x (2021).
119 Li, S. *et al.* Gasdermin D in peripheral myeloid cells drives neuroinflammation in experimental autoimmune encephalomyelitis. *J Exp Med* **216**, 2562-2581, doi:10.1084/jem.20190377 (2019).
120 McKenzie, B. A., Dixit, V. M. & Power, C. Fiery Cell Death: Pyroptosis in the Central Nervous System. *Trends Neurosci* **43**, 55-73, doi:10.1016/j.tins.2019.11.005 (2020).
121 Wu, Y. *et al.* Cell pyroptosis in health and inflammatory diseases. *Cell Death Discov* **8**, 191, doi:10.1038/s41420-022-00998-3 (2022).

Acknowledgements

We thank the members of the European Research Council ATTACK consortium for their discussion and Dr. Eric Espinosa and Dr. Cosima Baldari for their helpful critiques of this manuscript. We thank the flow cytometry and microscopy core facilities of the INSERM UMR 1037 (CRCT). This research has received funding from the European Research Council (ERC) under the European Union's Horizon 2020 Research and Innovation Programme (Grant agreement No. Syn- 951329). The research was also supported by INSERM institutional funding, from the Fondation Toulouse Cancer Santé and from the Oncopole Claudius-Regaud. Funders had no role in the preparation of this manuscript.

Author contributions

BM designed the research, performed experiments, analyzed results, and wrote the paper. MPP, FR, LD, EC, and SM performed experiments, analyzed data, and edited the paper. SV supervised the research, designed the project, and wrote the paper.

Competing interests

The authors declare they have no competing interests.

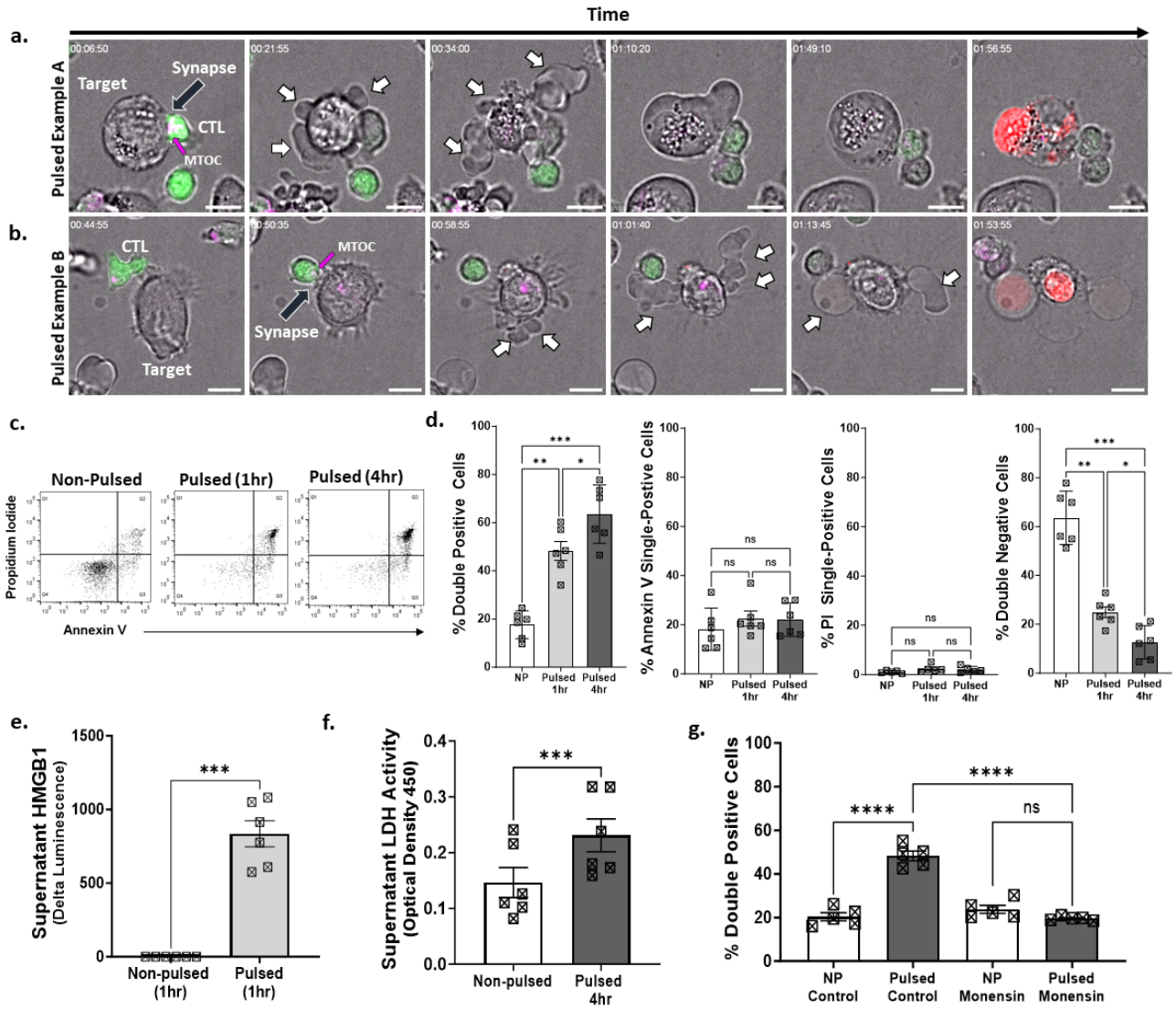

Figure 1 | Target cell death upon CTL attack resembles pyroptosis and is characterized by rapid erratic membrane bubbling, formation of pyroptotic bodies, loss of membrane integrity, and release of intracellular contents

a,b. JY target cells were pulsed with 10µM antigenic peptide, and conjugated at an E:T ratio of 1:1 with antigen-specific human CTLs pre-loaded with Fluo-8-AM (*green*) and SPY650 Tubulin (*magenta*) in the presence of 6.6µg/mL propidium iodide (*red*). Conjugate formation and cell death morphology was assessed using spinning disk time lapse microscopy for 2hr. Snapshots (from **Supplementary Movie 1** and **2**) illustrate various stages of CTL attack including initial CTL contact, MTOC polarization (*magenta arrows*), synapse formation (*black arrows*), pyroptotic body formation (*white arrows*), and loss of membrane integrity, indicated by PI entry. Two representative examples from n=3 independent experiments are shown; additional examples in **Supplementary Figure 1**. Scale bar is 10µm. **c,d.** JY cells were pulsed or non-pulsed (**NP**) with antigenic peptide and conjugated at an E:T ratio of 4:1 with antigen-specific human CTLs for 1 or 4 hours. Following conjugation, cells were subjected to Annexin V/PI staining and analyzed by flow cytometry. **c.** Representative dotplots of target cells from n=6 biological experiments are presented. **d**. Data shown represent the percentage of target cells in each quadrant (Annexin V/PI double positive, Annexin V single-positive, PI single-positive, or double negative) at the indicated time points. Individual datapoints represent the results of a single experiment. Bars represent the mean of n=6 biological experiments +/- SEM. RM one-way ANOVA with Tukey's test for multiple comparisons was utilized to assess statistical significance. **e.** Antigen-pulsed or non-pulsed JY cells were conjugated at a 4:1 E:T ratio with CTLs for 1hr and supernatants subjected to luminescent HMGB1 immunoassay. Results shown represent the difference in luminescence between pulsed and non-pulsed conditions. Individual datapoints represent the results of single experiment, while bars represent the mean of n=6 biological experiments +/- SEM. A paired *t*-test was utilized to assess statistical significance. **f.** Antigen-pulsed or non-pulsed JY cells were conjugated at a 4:1 E:T ratio with CTLs for 4hr and supernatants subjected to LDH activity assay. Results shown indicate OD450 values. Individual datapoints represent the results of single experiment, while bars represent the mean of n=6 biological experiments +/- SEM. A paired *t*-test was utilized to assess statistical significance. **g.** JY cells were pulsed or non-pulsed with antigenic peptide and conjugated at an E:T ratio of 4:1 with CTLs that had been pre-treated or not with monensin to de-acidify lytic granules. After 4hr conjugation, cells were subjected to Annexin V/PI staining and analyzed by flow cytometry. Data shown represent the percentage of target cells in the Annexin V/PI double-positive quadrant. Individual datapoints represent the results of single experiment, with a total of n=5 biological experiments. One-way ANOVA with Tukey's test for multiple comparisons was utilized to assess statistical significance. Bars represent mean of biological experiments +/- SEM. * $p<0.05$, ** $p<0.01$, *** $p<0.001$, **** $p<0.0001$, ns = non-significant.

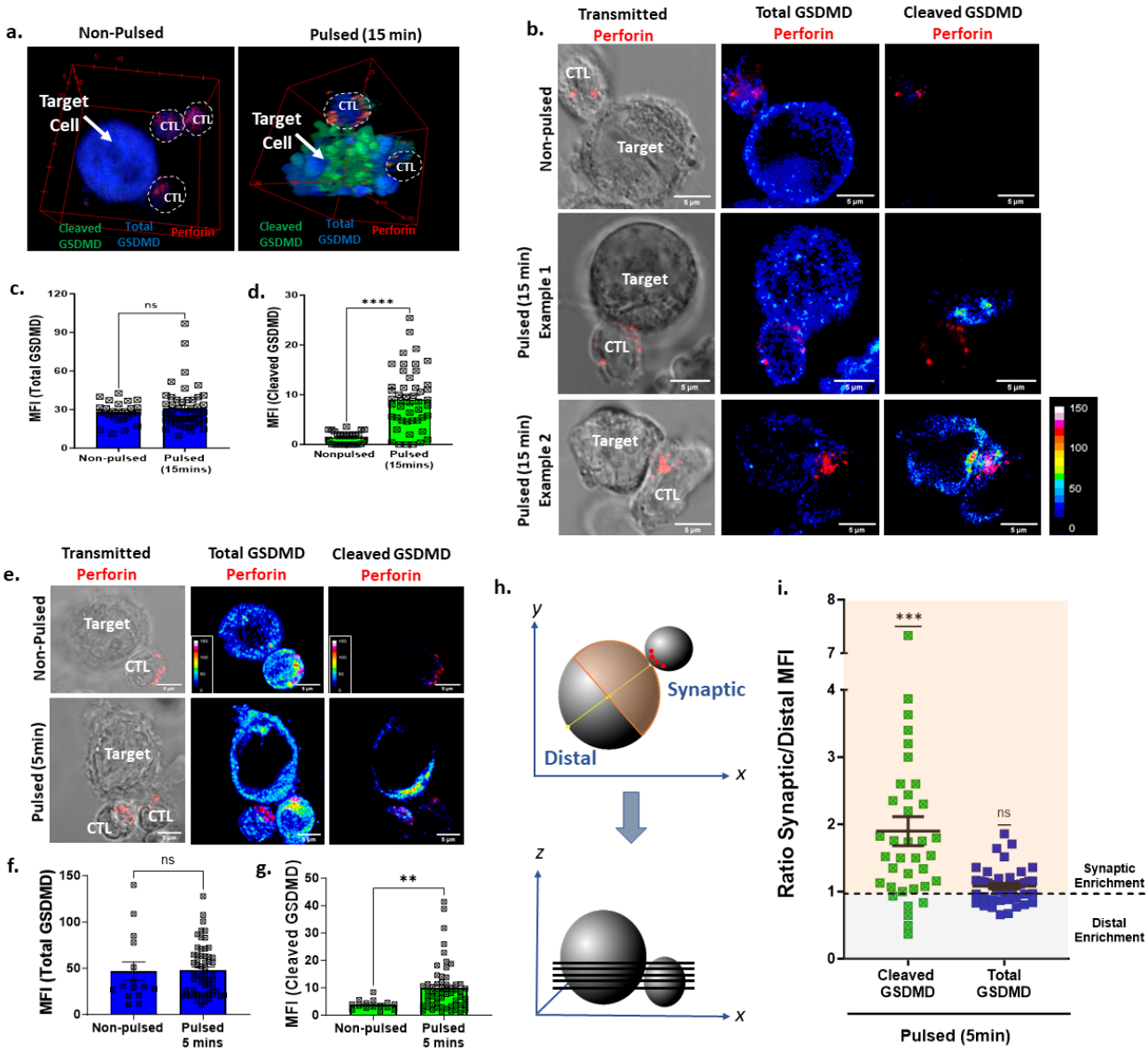

Figure 2 | Cleaved GSDMD is detectable upon CTL attack and is enriched adjacent to the synapse

a-d. JY target cells were pulsed with 10µM antigenic peptide and conjugated at an E:T ratio of 1:1 with antigen-specific human CTLs for 15min. Conjugates were fixed and subject to immunostaining for total GSDMD, cleaved GSDMD and perforin. **a.** 3D reconstruction with total GSDMD (*blue*), cleaved GSDMD (*green*) and perforin (*red*). **b.** Representative conjugates from non-pulsed and pulsed conditions, with total and cleaved GSDMD shown in pseudocolor and perforin in red. Images shown are from a single plane of the *z*-stack and are illustrative examples from n=4 biological experiments. **c.d.** Mean fluorescence intensity (MFI) of total and cleaved GSDMD within the target cell was measured manually on 5 different planes of the *z*-stack (separated by 1µm) at the height of the synpase and subsequently averaged. Each datapoint corresponds to one target cell, from n=4 biological experiments. Statistical differences between groups were assessed by unpaired *t*-tests. **e-g.** Target cells and CTLs were prepared as above and conjugated for 5min before being subjected to immunostaining and quantification as described. **h,i.** To assess whether cleaved or total GSDMD was enriched proximal to the synapse, each target cell was divided into two halves in the x-y plane (synaptic and distal) and MFI quantified separately for each half of the cell. This analysis was repeated across 5 planes of the z-stack and the average ratio of synaptic:distal signal for cleaved and total GSDMD was graphed as shown in **i.** Each datapoint shown represents a single cell. Mean ratio of synaptic:distal MFI for both cleaved and total GSDMD were compared to a hypothetical value of 1 (indicating even distribution of signal throughout the cell) using one-sample *t*-tests. Scale bars are 5µm. Error bars represent mean +/- SEM. ** $p<0.01$, *** $p<0.01$, **** $p<0.0001$, ns = non-significant.

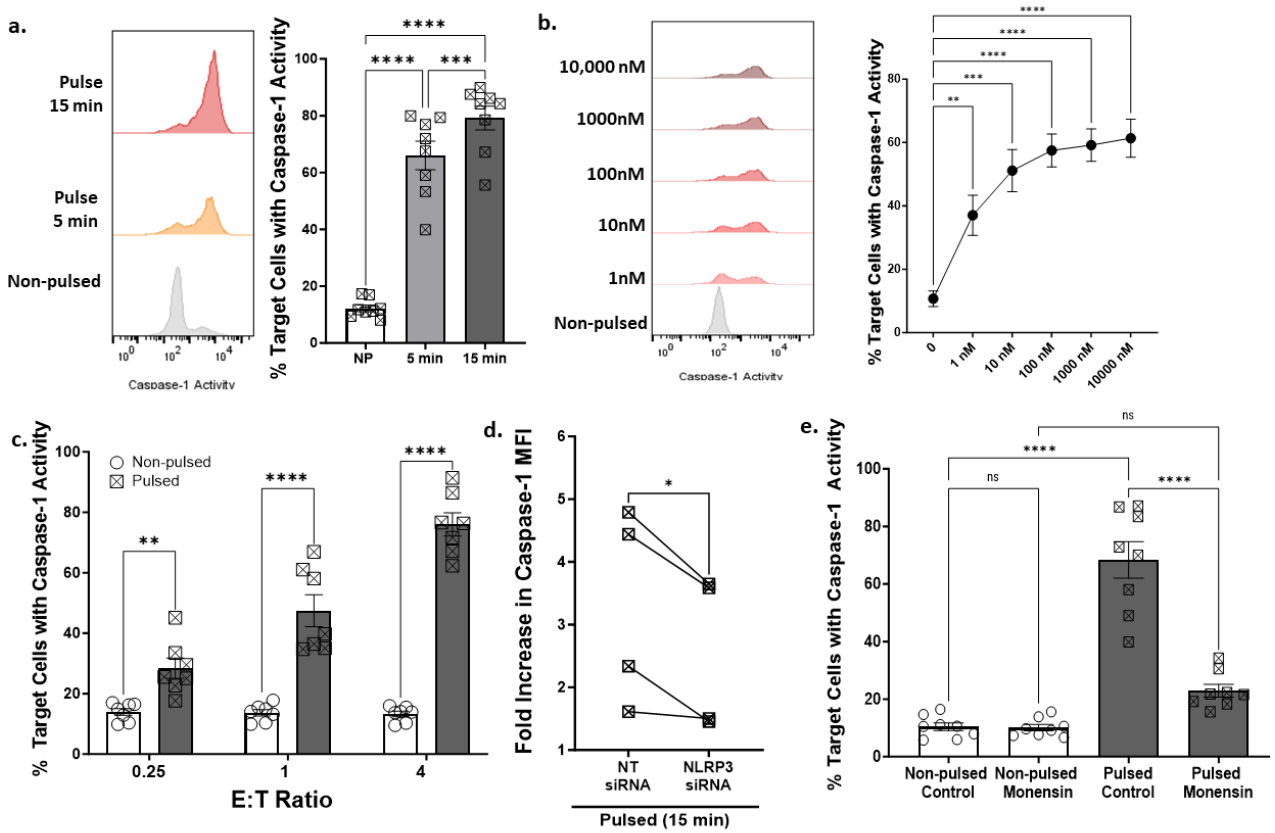

Figure 3 | The apical inflammatory caspase-1 is activated in JY target cells upon CTL attack downstream of target cell perforation and the NLRP3 inflammasome

a. JY target cells were pulsed or not with 10µM antigenic peptide and conjugated with CTLs at an E:T ratio of 4:1 for 5 or 15 min, before being stained with an activity-dependent caspase-1 probe and assessed using flow cytometry. Individual datapoints represent the results of single experiment, with a total of n=8 biological experiments. Bars represent mean +/- SEM. RM one-way ANOVA with Tukey's test for multiple comparisons was utilized to assess statistical significance. **b.** JY cells were pulsed with the indicated concentration of antigenic peptide at an E:T ratio of 4:1 for 15min and assessed as in **a.** Data shown represents mean +/- SEM, n=5 independent experiments. Ordinary one-way ANOVA with Tukey's test for multiple comparisons was utilized to assess statistical significance. **c.** JY cells were pulsed with 10µM antigenic peptide and conjugated with CTLs at the indicated E:T ratios for 15min and assessed as above. Individual datapoints represent the results of single experiment, with a total of n=7 biological experiments. Bars represent mean +/- SEM. Two-way ANOVA with Sidak's multiple comparison test was utilized to assess statistical significance. **d.** JY target cells were transfected with non-targeting (NT) or NLRP3-targeting siRNA for 24hr before being pulsed or not with 10µM antigenic peptide and conjugated with CTLs at an E:T ratio of 4:1 for 15 min. JY cells were stained with a caspase-1 probe as above. Data shown represents the average fold increase in caspase-1 median fluorescence intensity compared to non-pulsed controls for NT and NLRP3-targeting siRNA respectively (n=4 biological experiments). A paired *t*-test was utilized to assess statistical differences. **e.** JY cells were pulsed or non-pulsed with 10µM antigenic peptide and conjugated for 15min at an E:T ratio of 4:1 with CTLs that had been pre-treated or not with monensin to de-acidify lytic granules before being stained with an activity-dependent caspase-1 probe. Bars represent mean +/- SEM. Individual datapoints represent the results of single experiment, with a total of n=8 biological experiments. Ordinary one-way ANOVA with Tukey's test for multiple comparisons was utilized to assess statistical significance. *p<0.05, ** p<0.01, *** p<0.001, **** p<0.0001, ns = non-significant.

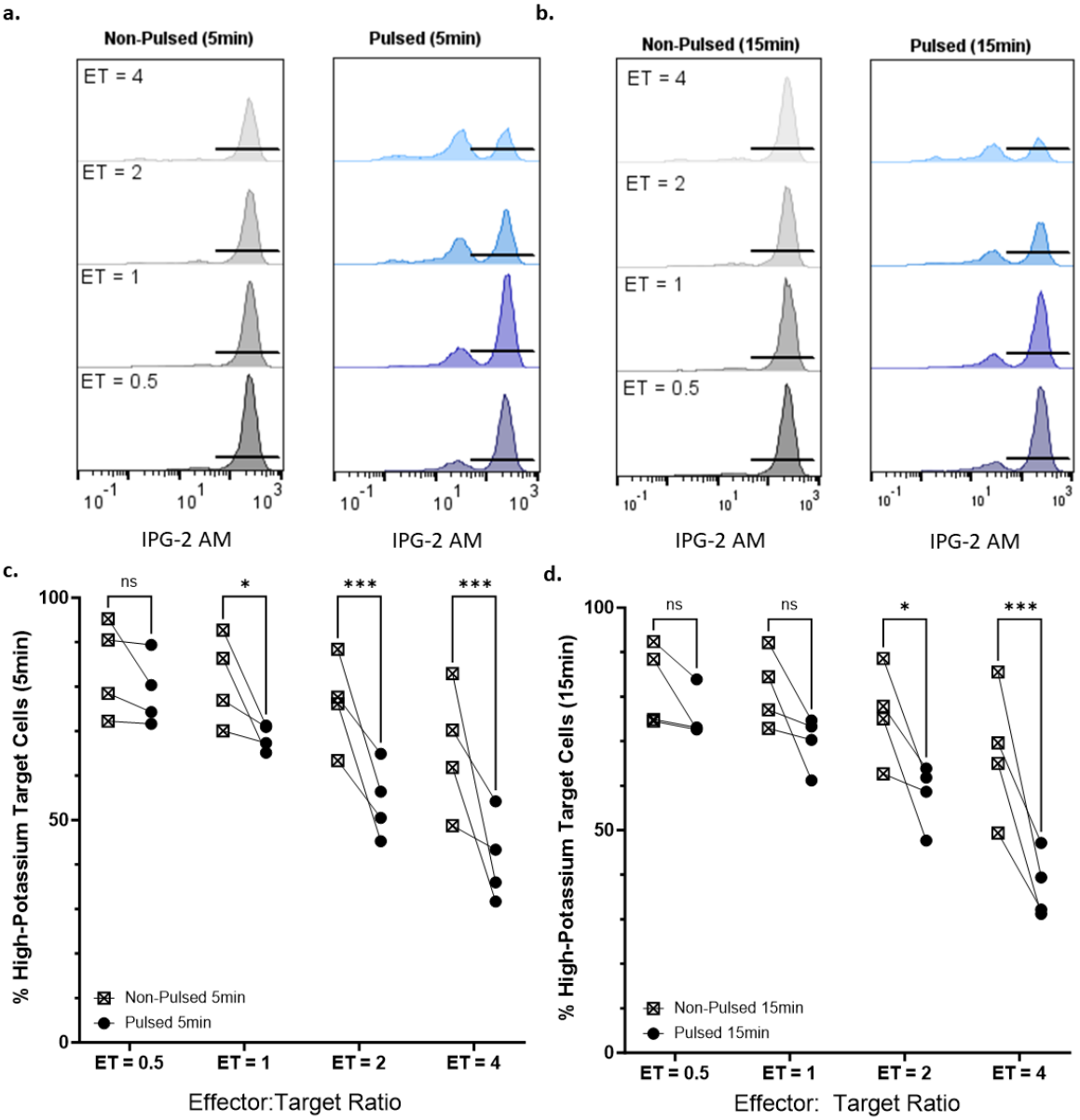

Figure 4 | Potassium efflux, a crucial initiator of NLRP3 inflammasome activity, is observed in target cells upon CTL attack
a,b. JY target cells were pulsed or not with 10μM antigenic peptide, stained with Ion Potassium Green (IPG-2 AM), conjugated with antigen-specific CTLs at the indicated E:T ratios for 5 or 15 min, and assessed using flow cytometry. Representative histograms are shown. **c,d.** Quantification of the percentage of cells in the high IPG-2 AM gate. Individual datapoints represent the results of single experiment, with a total of n=4 biological experiments. Bars represent mean +/- SEM. Two-way ANOVA with Dunnett's multiple comparison test was utilized to assess statistical significance. *p<0.05, ** p<0.01, *** p<0.001.

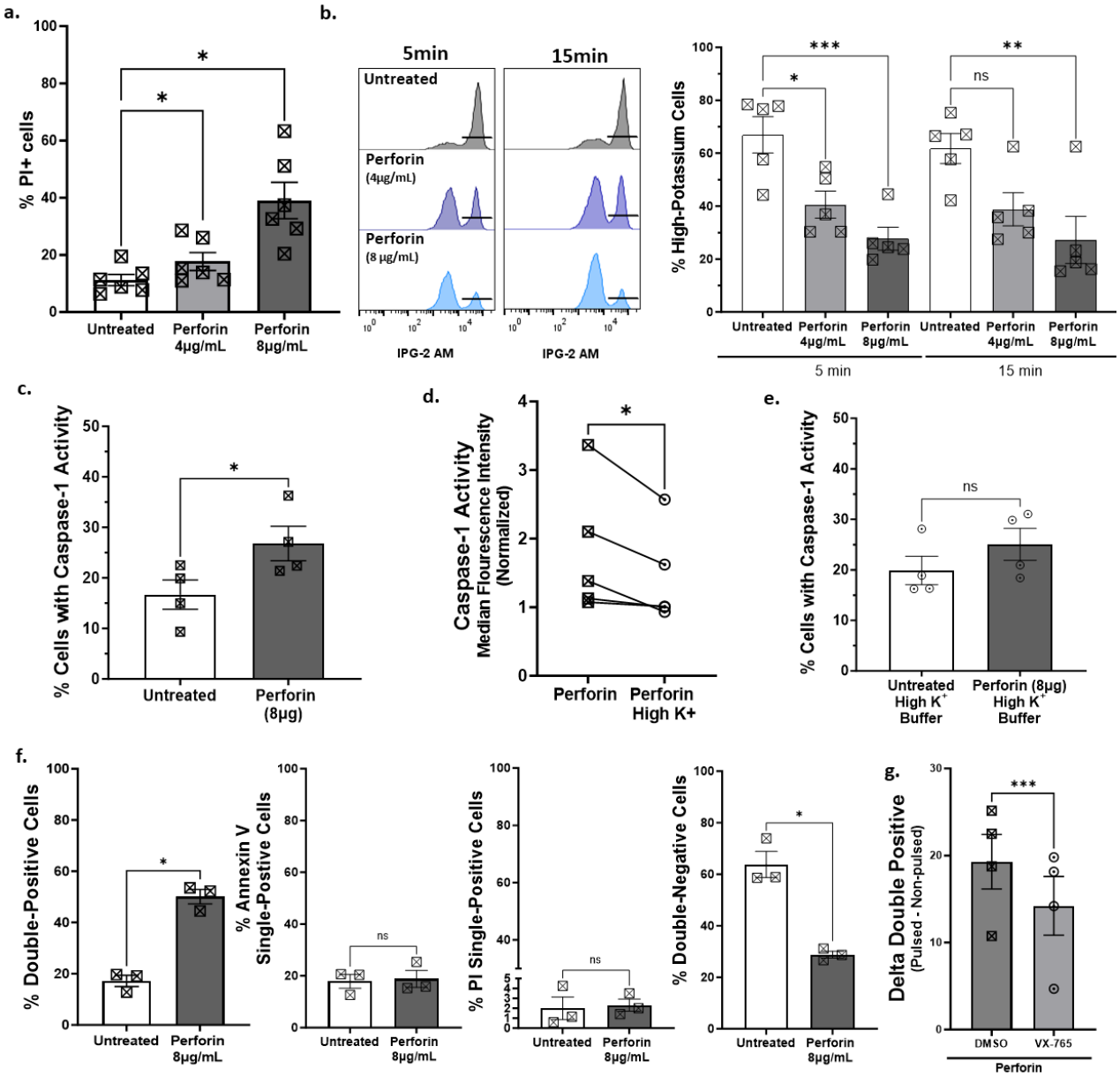

Figure 5 | Exogenous perforin triggers potassium efflux, caspase-1 activity, and pyroptosis in the absence of granzymes

a. JY target cells were treated with the indicated concentrations of recombinant human perforin in the presence of high-concentration extracellular PI (25µg/mL) for 15min in perforin binding buffer and the percentage of PI+ cells assessed by flow cytometry as a read-out of perforation. Individual datapoints represent the results of single experiment, with a total of n=6 biological experiments. Bars represent mean +/- SEM. RM one-way ANOVA with Tukey's test for multiple comparisons was utilized to assess statistical significance. **b.** JY target cells were preloaded with the fluorescent potassium indicator IPG-2 AM, treated with the indicated concentrations of recombinant human perforin for 5 and 15min in perforin binding buffer, and assessed by flow cytometry. Individual datapoints represent the results of single experiment, with a total of n=5 biological experiments. Bars represent mean +/- SEM. One-way ANOVA with Tukey's test for multiple comparisons was utilized to assess statistical differences. **c.** JY cells were pre-loaded with the activity-dependent caspase-1 probe in perforin binding buffer, treated with 8µg/mL recombinant human perforin for 30min and assessed by flow cytometry. Individual datapoints represent the results of single experiment, with a total of n=4 biological experiments. Bars represent mean +/- SEM. Paired t-test was utilized to assess statistical difference. **d,e.** In parallel, JY cells were pre-loaded with caspase-1 probe in high-potassium perforin binding buffer, treated with 8µg/mL recombinant human perforin for 30min and assessed by flow cytometry. Individual datapoints represent the results of single experiment, with a total of n=4 biological experiments. Bars represent mean +/- SEM. Paired *t*-test was utilized to assess statistical difference. **f.** JY target cells were treated with 8 µg/mL recombinant human perforin for 60min in perforin binding buffer, subjected to Annexin V/PI staining, and analyzed by flow cytometry. Individual datapoints represent the results of single experiment, with a total of n=3 biological experiments. Bars represent mean +/- SEM. Paired *t*-tests were utilized to assess statistical difference. **g.** JY cells were pre-treated with 100µM caspase-1 inhibitor VX-765 for 2hr before exposure to 8µg/mL recombinant human perforin for 60min. Cells were stained with Annexin V/PI and analyzed by flow cytometry. Datapoints shown represent the difference between control and perforin-treated conditions for solvent-treated and VX-765-treated cells, with a total of n=4 biological experiments. Paired *t*-tests were utilized to assess statistical difference. *$p<0.05$, ** $p<0.01$, *** $p<0.001$, ns = not significant.

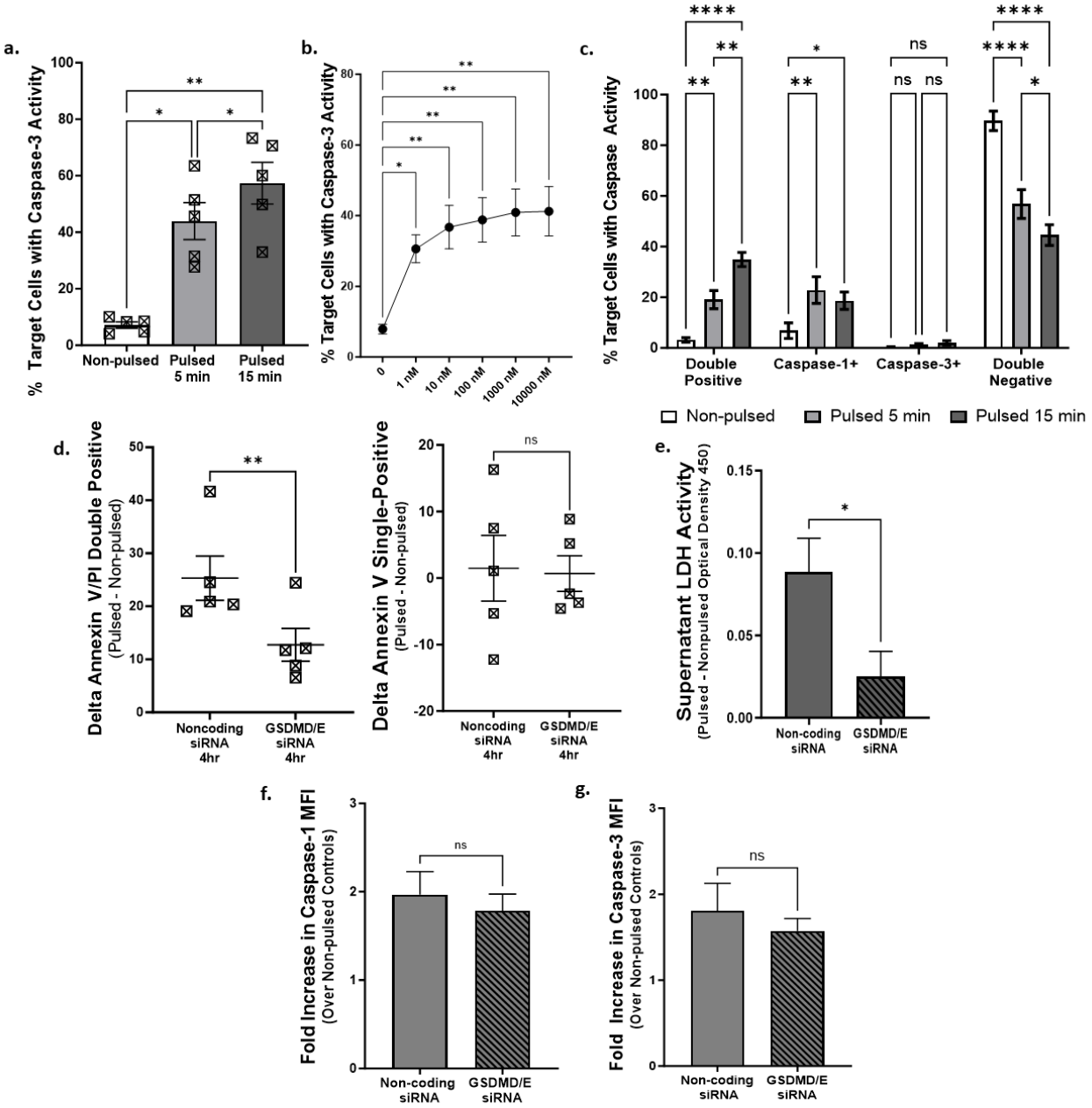

Figure 6| The caspase-3/GSDME pathway is activated in parallel to caspase-1/GSDMD to drive pyroptosis

a. JY target cells were pulsed or not with 10µM antigenic peptide and conjugated with CTLs at an E:T ratio of 4:1 for 5 or 15min, before being stained with an activity-dependent caspase-3 probe and assessed using flow cytometry. Individual datapoints represent the results of single experiment, with a total of n=5 biological experiments. Bars represent mean +/- SEM. RM one-way ANOVA with Tukey's test for multiple comparisons utilized to assess statistical significance. **b.** JY cells were pulsed with the indicated concentration of antigenic peptide at an E:T ratio of 4:1 for 15min and assessed as in **a.** Data shown represents mean +/- SEM, n=5 independent experiments. **c.** JY target cells were conjugated with CTLs as in **a** and double-stained for activity-dependent caspase-1 and caspase-3 probes before being assessed by cytometry. Cells were classified as single-positive, double-positive, or double-negative for each caspase at each timepoint shown. Bars represent mean +/- SEM. RM two-way ANOVA with Tukey's test for multiple comparisons was utilized to assess statistical significance. **d.** To assess the effect of inhibition of the GSDMD and GSDME pathways, JY cells were transfected with non-targeting siRNA or siRNAs targeting GSDMD and GSDME, before being pulsed with antigen, conjugated with antigen-specific CTLs for 4hrs, and subjected to analysis by Annexin V/PI staining and flow cytometry. Data shown represents the difference in the percentage of Annexin V/PI double-positive cells and Annexin V single-positive cells in the pulsed versus non-pulsed conditions after conjugation with CTLs. Paired *t*-tests were utilized to assess statistical significance. Data shown represents mean +/- SEM of n=5 biological experiments. **e.** Supernatants from a subset of experiments shown in **d** were collected after 4hr conjugation and subjected to LDH assay. Data shown represent the difference in supernatant LDH activity in the pulsed versus non-pulsed conditions after 4hr conjugation with CTLs. Bars represent mean +/- SEM. Paired *t*-tests were utilized to assess statistical significance, n=4 biological experiments. **f, g.** To assess whether GSDMD/E knockdown affected upstream activity of their respective caspases, cells transfected as in **d,e** were conjugated for 15min with CTLs and subjected to activity-dependent caspase-1 and -3 assays. Data represent fold increase in MFI for each caspase probe, normalized to respective non-pulsed controls. Bars represent mean +/- SEM. Paired *t*-tests were utilized to assess statistical significance, n=4 biological experiments. *p<0.05, ** p<0.01, *** p<0.001, **** p<0.0001, ns = not significant.

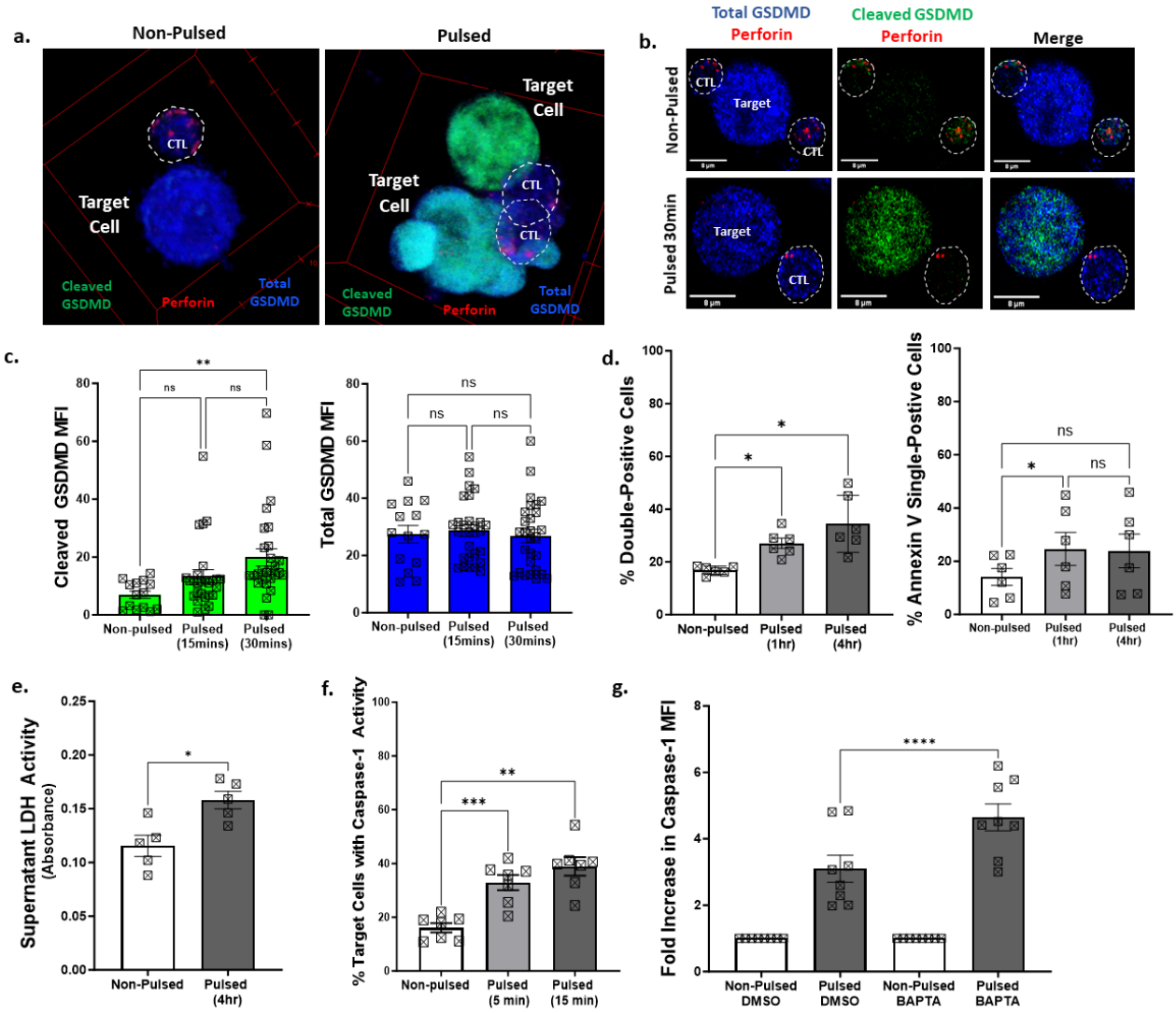

Figure 7 | D10 melanoma cells activate the canonical pyroptotic signaling pathway upon CTL attack, which is enhanced upon inhibition of calcium-dependent membrane repair mechanisms

a-c. D10 target cells were pulsed with 10µM antigenic peptide and conjugated at an E:T ratio of 1:1 with antigen-specific human CTLs for 15 or 30min. Conjugates were fixed and subject to immunostaining for total GSDMD, cleaved GSDMD and perforin. **a.** 3D reconstruction with total GSDMD (*blue*), cleaved GSDMD (*green*) and perforin (*red*). **b.** Representative conjugates from non-pulsed and pulsed conditions, with total GSDMD shown in blue, cleaved GSDMD shown in green, and perforin in red. Images shown are from a single plane of the *z*-stack and are illustrative examples from n=4 biological experiments. **c.** Mean fluorescence intensity (MFI) of total and cleaved GSDMD within the target cell was measured on 5 different planes of the *z*-stack (separated by 1µm) at the height of the synpase and subsequently averaged. Each datapoint corresponds to one target cell, drawn from n=4 biological experiments. Statistical differences between groups were assessed by ordinary one-way ANOVA with Tukey's test for multiple comparisons. **d.** D10 cells were pulsed or non-pulsed (NP) with antigenic peptide and conjugated at an E:T ratio of 4:1 with antigen-specific human CTLs for 1 or 4hr. Following conjugation, cells were subjected to Annexin V-PI staining and analyzed by flow cytometry. Data shown represent the percentage of D10 cells in the Annexin V/PI double positive quadrant and the Annexin V single-positive quadrant respectively at the indicated time points. Individual datapoints represent the results of single experiment, with a total of n=6 biological experiments. Bars represent mean +/- SEM. RM one-way ANOVA with Tukey's test for multiple comparisons was utilized to assess statistical significance. **e.** Antigen-pulsed or non-pulsed D10 cells were conjugated at a 4:1 E:T ratio with CTLs for 4hr and supernatants subjected to LDH activity assay. Results shown indicate OD450 values. Individual datapoints represent the results of single experiment, with a total of n=5 biological experiments. A paired *t*-test was utilized to assess statistical significance. **f.** D10 target cells were pulsed or not with 10µM antigenic peptide and conjugated with CTLs at an E:T ratio of 4:1 for 5 or 15min, before being stained with an activity-dependent caspase-1 probe and assessed using flow cytometry. Individual datapoints represent the results of single experiment, with a total of n=7 biological experiments. Bars represent mean +/- SEM. RM one-way ANOVA with Tukey's test for multiple comparisons was utilized to assess statistical significance. **g.** D10 cells were pre-treated with the calcium chelator BAPTA-AM to disable calcium-dependent membrane repair mechanisms or DMSO solvent control before being pulsed and conjugated with antigen-specific CTLs for 15min and subjected to caspase-1 activity assay. Data represent fold increase in caspase-1 MFI, normalized to respective non-pulsed controls. Bars represent mean +/- SEM. RM one-way ANOVA with Tukey's test for multiple comparisons was utilized to assess statistical significance, n=8 biological experiments. *p<0.05, ** p<0.01, *** p<0.001, ns = not significant.